# SPECTRAL ANALYSIS OF THE A2384 GALAXY CLUSTER AND THE BRIDGE BETWEEN GALAXY CLUSTERS

by

Elif Naz Toktaş

B.S., Physics, Boğaziçi University, 2022

Submitted to the Institute for Graduate Studies in
Science and Engineering in partial fulfillment of
the requirements for the degree of
Master of Science

Graduate Program in Physics
Boğaziçi University
2025

# ACKNOWLEDGEMENTS

First and foremost, I would like to express my sincere gratitude to my supervisor, Prof. E. Nihal Ercan. Her support, endless patience, and invaluable guidance, starting from my undergraduate years and continuing through every stage of my academic journey, have played a fundamental role in shaping my path in high-energy astrophysics. I am truly thankful for her belief in me, which has always motivated me and helped me stay on track.

I would like to sincerely thank Sinancan Kara (very-soon-to-be Dr.), who patiently taught us how to analyze XMM-Newton data at the bottom of the ladder. His guidance was essential in helping us learn all these analysis.

This learning process was not something I went through alone, and I feel truly lucky to have met Binnur, İsmet, and Gökhan along the way. From the early days of figuring things out together to the point where each of us followed our own paths in different fields, the journey we shared has always held a special meaning for me. I owe a heartfelt thank you to them, who have stood by me not only throughout this thesis but in so many areas of life since the day we met. Without their support and presence, I might not have believed I was capable of achieving something of this scale. Their encouragement stands me up when I needed it most.

I would also like to express my deepest gratitude to my mom and dad. They supported my fascination with space from the very beginning, and opened the door to a lifelong passion by sending me to space camp when I was a child. I am truly grateful for their belief in me and their constant support.

I dedicate this thesis to my siblings Merve Nil and Yavuz, who asked me, ”Sister, how long will you continue to do these projects?” My answer: maybe for a lifetime.

# ABSTRACT


## SPECTRAL ANALYSIS OF THE A2384 GALAXY CLUSTER AND THE BRIDGE BETWEEN GALAXY CLUSTERS

Galaxy clusters are massive structures bound by gravitational attraction, consisting of hundreds or even thousands of individual galaxies. As one of the largest structures in the universe, galaxy clusters are extremely rich in both ordinary (baryonic) and dark matter. The member galaxies within a galaxy cluster, along with dark matter and the hot gas spread throughout the cluster, are bound together under a significant gravitational potential. The hot gas found within galaxy clusters is called the "Intracluster Medium" (ICM), which, due to events like SNcc and SNIa supernova explosions occurring within the cluster, becomes chemically enriched and can reach temperatures of millions of degrees. This high temperature within the cluster causes the gas to emit strong X-rays, allowing us to study the temperature, metallicity, entropy, and chemical composition of the ICM through X-ray observations.

In this study, the post-merger galaxy cluster known as Abell 2384 ($z \approx 0.0943$) is examined. The XMM-Newton/EPIC and Chandra/ACIS-I observations of the A2384(S) and A2384(N) clusters, as well as the bridge between them, have been analyzed, and temperature and metallicity profiles are presented. The models indicate that the Bridge 1 and Bridge 2 regions are hotter, more active, and more metal-rich compared to the A2384(S) and A2384(N) regions. Furthermore, models based on data obtained from Chandra and XMM-Newton observations show that the metallicity increases as one approaches the A2384(S) region, but this increase starts to decrease as one moves further into the A2384(S) region. This suggests the need for a more detailed investigation of the radio source mentioned in previous studies.

# ÖZET

## A2384 GALAKSİ KÜMESİNİN VE GALAKSİ KÜMELERİ ARASINDAKİ KÖPRÜNÜN SPEKTRAL ARAŞTIRMASI

Galaksi kümeleri, içerlerinde yüzlerce hatta binlerce galaksi barındıran ve kütleçekimsel kuvvet sayesinde bir arada tutlan yapılardır. Evrenin en büyük yapılarından biri olan galaksi kümeleri, hem sıradan (baryonik) hem de karanlık madde açısından son derece zengin yapılardır. Galaksi kümesinin içerisinde bulunan üye galaksiler, karanlık madde ve küme içine yayılmış sıcak gazla birlikte büyük bir kütleçekimsel potansiyel altında bir arada tutulur. Galaksi kümelerinin barındırdığı sıcak gaz ”küme içi ortam” (Intracluster Medium, ICM) olarak adlandırılır, bu gaz kümenin içerisinde gerçekleşen SNcc ve SNIa süpernova patlamaları gibi olaylarla kimyasal açıdan zenginleşmenin yanısıra sıcaklık olarak milyon derecelere kadar ısınabilmektedir. Küme içindeki bu yüksek sıcaklık, güçlü X-ışınları yayılmasına neden olur ve bu sayede X-ışını gözlemleri aracılığıyla, küme içi ortamın sıcaklık, metallik, entropi ve kimyasal bileşimi hakkında bilgi edinebiliriz.

Bu çalışmada, birleşme sonrası galaksi kümesi olarak bilinen Abell 2384 ($z \approx 0.0943$) incelenmektedir. A2384(G) ve A2384(K) kümeleri ile bu kümeler arasında uzanan köprünün XMM-Newton/EPIC ve Chandra/ACIS-I gözlemleri analiz edilmiş ve sıcaklık ile metal bolluğu profilleri sunulmuştur. Yapılan modellemeler, Köprü 1 ve Köprü 2 bölgelerinin, A2384(K) ve A2384(G) bölgelerine kıyasla daha sıcak, daha aktif ve metal açısından daha zengin olduğunu göstermektedir. Ayrıca, Chandra ve XMM-Newton gözlemleriyle elde edilen verilere dayalı modellemeler, A2384(G) bölgesine yaklaştıkça metal bolluğunun arttığını, ancak bu artışın A2384(G) bölgesine doğru azalmaya başladığını ortaya koymaktadır. Bu durum, önceki çalışmalarda da belirtilen radyo kaynağının daha ayrıntılı bir şekilde incelenmesi gerektiğine işaret etmektedir.

# TABLE OF CONTENTS

# LIST OF FIGURES

# LIST OF TABLES

# LIST OF SYMBOLS

| | |
|---|---|
| $D_A$ | Angular size distance |
| $g_{ff}$ | Gaunt factor |
| $n_i$ | Ion density |
| K | Kelvins |
| kpc | Kiloparsecs |
| $M_\odot$ | Solar mass |
| Mpc | Megaparsecs |
| $n_e$ | Electron density |
| $n_H$ | Hydrogen column density |
| $T_g$ | Gas temperature |
| $Z_\odot$ | Solar abundance |
| $z$ | Redshift |
| | |
| $\Delta E$ | Excitation energy |
| $\epsilon_\nu$ | X-ray emissivity at frequency $\nu$ |
| $\mu$ | Mean molecular mass |
| $\nu$ | Frequency |
| $\Omega$ | Collisional strength |
| $\omega$ | Statistical weight |

# LIST OF ACRONYMS/ABBREVIATIONS

| | |
|---|---|
| A2384 | Abell 2384 |
| ACIS | Advanced CCD Imaging Spectrometer |
| ACT | Atacama Cosmology Telescope |
| AGN | Active Galactic Nucleus |
| ARF | Ancillary Response File |
| ATHENA | Advanced Telescope for High Energy Astrophysics |
| BCG | Brightest Cluster Galaxy |
| CCD | Charge-coupled Device |
| CCF | Current Calibration Files |
| CDA | Chandra Data Archive |
| CIAO | Chandra Interactive Analysis of Observations |
| CIE | Collisional ionization Equilibrium |
| CXB | Cosmic X-ray Background |
| DS9 | SAOImageDS9 |
| DSS | Digitized Sky Survey |
| EPIC | European Photon Imaging Camera |
| ESA | European Space Agency |
| ESAS | Extended Source Analysis Software |
| FPA | Focal Plane Assembly |
| GMRT | Giant Metrewave Radio Telescope |
| HRC | High Resolution Camera |
| ICM | Intracluster Medium |
| HEASARC | High Energy Astrophysics Science Archive Research Center |
| keV | Kiloelectron-volts |
| MOS | EPIC Metal-Oxide Semiconductor Detector |
| MSP | Mirror Support Platform |
| NASA | National Aeronautics and Space Administration |
| NED | NASA/IPAC Extragalactic Database |

| | |
|---|---|
| ODF | Observation Data Files |
| OM | Optical Monitor |
| PN | EPIC PN-junction Semiconductor Detector |
| pp | proton-proton chain |
| RGA | Reflection Grating Assembly |
| RGS | Reflection Grating Spectrometer |
| RMF | Response Matrix File |
| SAS | Science Analysis System |
| SB | Surface Brightnessa |
| SIM | Science Instrument Module |
| SNcc | Core Collapse Supernova |
| SNIa | Supernova Type-Ia |
| SPT | South Pole Telescope |
| SVM | Service Module |
| SZ | Sunyaev–Zel'dovich |
| XMM | X-ray Multi-Mirror Mission |
| XSPEC | X-ray Spectral Fitting Program |

# 1. INTRODUCTION

The universe, along with all matter and energy within it, was created in an event known as the "Big Bang", which occurred approximately 13.8 billion years ago. It contains complex and hierarchical structures such as galaxies, stars, planets and other celestial bodies. In addition to these structures, the observable universe is dominated by dark energy (∼68%) and dark matter (∼27%), and baryonic matter has a share of ∼5% [1]. Among these structures, galaxy clusters are the largest gravitationally bound structures in the universe, and these giant systems consisting of hundreds or even thousands of galaxies are extremely rich in both ordinary (baryonic) and dark matter. Galaxies within a cluster are held together under a large gravitational potential together with dark matter and the surrounding hot gas. While a significant portion of the baryonic matter is found in the hot gas known as the intracluster medium (ICM) distributed throughout the cluster [2] and whose temperature can reach millions of degrees Kelvin, dark matter is found near the central region of the galaxy cluster [3], and as a result, the heated gas emits X-rays.

X-ray observations play a crucial role in studying galaxy clusters, as they provide information about the temperature, metallicity, entropy, and chemical composition of the ICM. Additionally, these observations allow for the mapping of the large-scale structure of the Universe and the study of how baryonic matter interacts with dark matter within clusters [4, 5].

The ICM, in an attempt to regain equilibrium under gravitational influence, begins to show differentiation in terms of temperature, density, and metallicity. The dense gas is enriched through the effects of core-collapse supernovae (SNcc) and Type Ia supernovae (SNIa), providing critical insights into the chemical history of galaxy clusters [6]. These variations in chemical composition and thermodynamic state across the ICM reflect the cumulative effects of merger dynamics, gas stripping, and star formation over the cluster's history.

The study by Maurogordato et al. [7] emphasized how the merging of these two subclusters affects the dynamic distribution of hot gas within the ICM. In this thesis, we also aim to observe and analyze the changes in the ICM caused by the merging process, as well as the metallicity and individual element profiles, using observations from the XMM-Newton and Chandra satellites. By leveraging the complementary strengths of these observatories, we aim to construct a detailed picture of the thermodynamic and chemical evolution of A2384 and its connection to large-scale structure formation in the Universe.

In this thesis, we focus on the galaxy cluster Abell 2384 (A2384), which has a redshift value of $z \approx 0.0943$ in total, $z \approx 0.0942$ in the North and $z \approx 0.0946$ in the South [8]. This cluster consists of two subclusters, referred to as A2384(N) and A2384(S), which are observed to be connected by a hot, X-ray-emitting gas bridge approximately 700 kpc in length [9, 10]. Past studies show that A2384 exhibits post-merger characteristics [11].

## 1.1. Galaxy Clusters & Merging Galaxy Clusters

In this chapter, we will first define the galaxy clusters, merging galaxy clusters, their historical background, and then we will investigate the basic properties of galaxy clusters. Later, we will look at the basic properties of ICM and X-ray studies regarding galaxy clusters from the past to now.

### 1.1.1. Observation History of Galaxy Clusters

Throughout human history, the night sky has been a source of fascination and mystery. Before the invention of the telescope, only bright stars and planetary motions were visible to the naked eye. With telescopic astronomy, countless points of light were resolved into stars, nebulae, and later, entire galaxies. Among these, galaxy clusters, gravitationally bound systems of hundreds or thousands of galaxies, emerged as key cosmological structures.

The study of clusters spans more than three centuries, evolving from early optical observations to high-resolution, multi-wavelength surveys that probe the dynamics, composition, and large-scale distribution of matter in the universe. Systematic observations of non-stellar objects began in the $18^{th}$ century.

Charles Messier's 1774 "catalogue of nebulae" and star clusters, compiled to distinguish them from comets, was extensive. Many of these entries were later recognized as galaxies or galaxy groups. In the late 1700s, William Herschel conducted comprehensive star surveys and proposed that the Milky Way had a disk-like structure surrounded by other nebular systems, suggesting an early concept of exogalaxies or "island universes" [12].

In 1750, the English astronomer Thomas Wright proposed that the appearance of the Milky Way as a luminous band in the sky could be explained if it were a flattened disk of stars, seen from within. In his treatise *An Original Theory or New Hypothesis of the Universe*, Wright also speculated that other such "nebulae" might be distant systems similar to the Milky Way, an early conceptual precursor to the idea of galaxies as island universes [13]. Although his ideas were largely philosophical and lacked observational support, they influenced later thinkers such as Immanuel Kant.

The question of whether spiral nebulae like Andromeda were part of the Milky Way or distant systems sparked intense debate in the early $20^{th}$ century, known as "the Great Debate" between Harlow Shapley and Heber Curtis. This controversy was resolved in the 1920s through the work of Edwin Hubble. Using the 100-inch Hooker Telescope at Mount Wilson Observatory, Hubble identified *Cepheid variable stars* in the Andromeda nebula which is well known M31 and, by applying Henrietta Leavitt's period-luminosity relation, Hubble placed M31 well outside the bounds of the Milky Way, proving it to be an independent galaxy [14]. This contribution, enabled the classification of galaxies by morphology (spiral, elliptical, irregular), and laid the groundwork for the Hubble sequence and the concept of large-scale structure. Hubble's this discovery established that the universe contained numerous galaxies beyond our own, fundamentally changing our cosmic perspective.

Figure 1.1. The image above shows the Coma Galaxy Cluster (Abell 1656) in the optical band. This cluster is one of the earliest examples of rich galaxy clusters and is included in the Abell catalog. In 1933, Fritz Zwicky studied the motions of galaxies within this cluster and was the first to propose the existence of dark matter. Credit: ESA/ESASky, DSS2 [15].

A decade later, Fritz Zwicky conducted a dynamical study of the Coma Cluster (Abell 1656), a rich cluster of galaxies located over 300 million light-years away. By measuring the redshifts of individual galaxies and applying the virial theorem, Zwicky calculated the total mass required to keep the system gravitationally bound. He found that the luminous mass, estimated from the brightness of the galaxies, was at least an order of magnitude smaller than required by the virial equilibrium. To reconcile this discrepancy, he proposed the presence of a substantial unseen mass, which he called "dark matter" [16]. Although his proposal was initially ignored for years, Zwicky's work is now recognized as the first quantitative evidence for the existence of dark matter. His analysis also foreshadowed the importance of velocity dispersion and gravitational lensing in studying mass distributions in clusters.

A major step in the study of galaxy clusters came with George O. Abell's *Catalogue of Rich Clusters of Galaxies*, published in 1958 [17]. His systematic approach enabled the first large-scale statistical analyses of cluster abundance, distribution, and spatial clustering. The catalog listed 2,712 rich clusters in the northern hemisphere, selected based on richness and compactness.

Abell also introduced the concept of richness classes (0 to 5) and estimated redshifts using the median magnitude method. His definitions, including the *Abell radius* and *richness class*, remain standard tools in extragalactic astronomy. The catalog was later extended to the southern sky by Abell, Corwin, and Olowin in 1989, forming the Abell–ACO catalog [18].

Building upon these foundational discoveries, the X-ray-emitting plasma, first discovered by the Uhuru satellite [19], contributed to our understanding of the nature of the hot gas, which constitutes the majority of the baryonic matter in galaxy clusters.

Subsequent observations with X-ray telescopes such as Einstein, ROSAT, XMM-Newton, and Chandra have deepened the investigations of galaxy clusters. The Einstein Observatory (1978–1981) and ROSAT (1990–1999) improved spatial and spectral resolution, allowing studies of cooling flows, where dense central regions of clusters radiate energy, and the identification of substructures and scaling relations such as the $L_X - T$ relation [20, 21].

The Chandra and XMM-Newton missions, launched in 1999, enabled high-resolution imaging and spectroscopy of clusters. Chandra uncovered sharp structures such as cold fronts and AGN-inflated cavities, while XMM-Newton provided detailed metallicity and temperature profiles [22, 23]. During the same period, the Sunyaev–Zel'dovich (SZ) effect became a vital tool for cluster detection, independent of redshift. Experiments like Planck, Atacama Cosmology Telescope (ACT), and South Pole Telescope (SPT) used the SZ effect to build large cluster catalogs, improving constraints on cosmological parameters [24].

In 2019, the launch of eROSITA initiated the most sensitive all-sky X-ray survey since ROSAT. eROSITA aims to detect more than 100,000 galaxy clusters, enabling robust measurements of the evolving mass function and large-scale structure [25].

Looking ahead, the Advanced Telescope for High Energy Astrophysics (ATHENA) mission, planned for the late 2030s, is expected to significantly advance X-ray spectroscopy. Its instruments will investigate turbulence, gas dynamics, and metal enrichment in the ICM at redshifts up to $z > 2$ [26].

### 1.1.2. Galaxy Clusters

Galaxy clusters are the largest gravitationally bound structures in the universe. These colossal systems, comprising hundreds or even thousands of galaxies, are extremely rich in both ordinary (baryonic) and dark matter. The galaxies within a cluster, along with dark matter and the surrounding hot gas, are held together under a large gravitational potential. The primary sources of the chemical enrichment of galaxy clusters, which have been enriched chemically over billions of years by their member galaxies, are supernova explosions known as core-collapse supernovae (SNcc) and Type Ia supernovae (SNIa) [2, 6].

During SNcc explosions, which occur when stars with a mass of at least 8-10 solar masses undergo core collapse, a significant amount of alpha elements such as Fe, O, Ne, Mg, S, and Si are released into the intracluster medium (ICM) [27]. Additionally, during SNIa explosions, which are triggered by the explosion of low-mass white dwarf stars, iron-peak elements such as Fe, Ni, and Co are produced [28]. The shock waves generated during these explosions heat the ICM and enhance the thermal bremsstrahlung radiation, which dominates X-ray observations [4, 27]. The heavy elements ejected from galaxies due to supernova explosions in member galaxies enrich the ICM. Unlike stars, the majority of the baryonic matter in galaxy clusters exists in the form of hot, ionized gas within the cluster's medium. This gas also acts as a reservoir for the cumulative effects of star formation, supernova feedback, and AGN activity across cosmic time [5, 6, 27].

X-ray observations are among the most powerful tools for understanding the thermal structure of the ICM and the processes that contribute to its enrichment.

In particular, detailed spectroscopic studies provide constraints on the relative contributions of SNcc and SNIa to the chemical composition of the ICM, thereby enabling constraints on the star formation history and the evolutionary state of clusters [6, 27].

### 1.1.3. Merging Galaxy Clusters

Post-merger systems are clusters that are still undergoing active gravitational evolution. During the collision of galaxy clusters, the energy released creates significant shock waves and turbulence, leading to a partially irregular structure. These shock waves compress and heat the gas within the cluster and increase turbulence, which in turn affects the metallicity profiles of the ICM [29]. The study of post-merger systems like A2384 provides an excellent opportunity to investigate how gravitational interactions shape the thermodynamic and chemical properties of the ICM.

Merging events occur in multiple stages. In the initial stage, clusters are accelerated due to gravitational attraction, creating compression and shock waves in the ICM. Such phenomena lead to high temperatures and irregular density profiles during the early stages of merging [30]. In the later stages of merging, due to shock waves and turbulence, the gas within the ICM acquires an irregular structure, causing large-scale variations in temperature and metal distribution [31]. By examining the interaction of shock waves with cold fronts in galaxy clusters, the contribution of these processes to the gas distribution within the ICM can be explained in detail [29]. This interaction also impacts cooling mechanisms in the ICM, potentially influencing the star formation rate and feedback processes in cluster galaxies [5].

### 1.1.4. Galaxy Cluster's Merging Stages

As we mentioned in the previous section, galaxy clusters are the largest gravitationally bound structures in the universe, while merging of galaxy clusters are one of the most energetic events in the universe where we can observe hierarchical growth.

Cluster mergers are among the most violent events in the universe, releasing energy on the order of $10^{63}$–$10^{64}$ ergs [32]. The shock waves and turbulence generated during these high-energy collisions give rise to large-scale synchrotron structures (radio halos and relics) at radio wavelengths [33, 34]. These merger processes not only drive the mass growth of clusters, but also greatly change the physical properties of the intracluster medium (ICM), such as temperature, density, metal abundance, and magnetic field. [35].

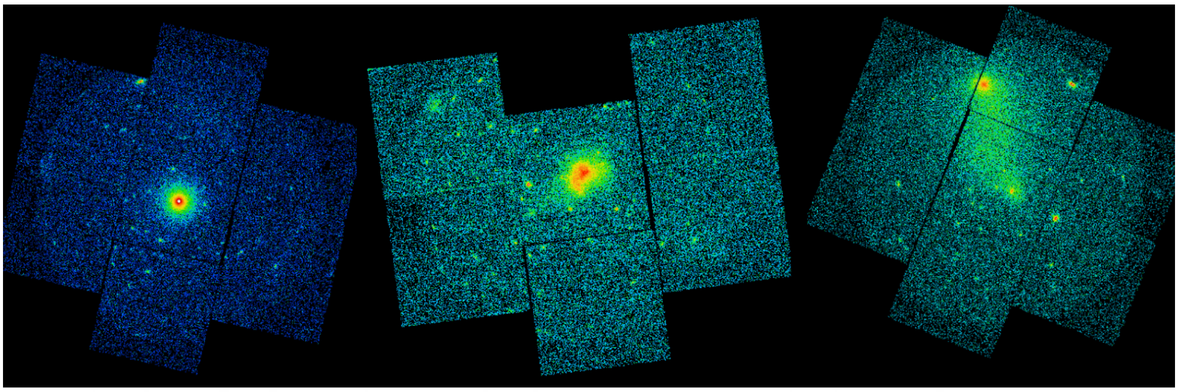

Figure 1.2. A383 (left), MACS J0717.5+3745 (center) and A2384 (right) are examples of cooling flow [36] , pre-merging [37] and post-merged [38] clusters of galaxies. Images are taken from XMM-Newton Science Archive [39].

The merging process of galaxy clusters is studied in three main stages:

(i) Pre-Merging Stage
(ii) Merging Stage
(iii) Post-Merging Stage

The pre-merging stage is when two or more galaxy clusters begin to gravitationally approach each other. This phase is called pre because the nuclei have not yet collided [40]. During this phase, the morphology and intracluster environment of galaxy clusters, which structurally preserve their own properties, are stable. However, in some cases, there may be a small interaction between ICMs, but this is usually limited to the asymmetries observed only in the outer layers [29].

Since only the approach and small-scale interactions occur during this phase, synchrotron events such as haloes or relics are not observed in radio observations [33]. In X-ray observations, more regular and symmetrical emissions are observed [41]. Studying this phase is critical to understanding the initial conditions of cluster merger and how it may continue.

The merging stage is the most violent of these phases. The nuclei of galaxy clusters collide, and during this process, strong shock waves and turbulence are generated in the intracluster medium (ICM), which leads to significant changes in thermal and non-thermal components [29, 32]. The shock waves formed after this energetic event heat the ICM, causing a temperature increase, while the particles are re-accelerated by turbulence, which leads to the formation of large-scale synchrotron structures at radio wavelengths [35]. Radio halos and radio relics are frequently observed [33, 41].

In the merging phase, the galaxies in the galaxy clusters whose galaxy distributions are disrupted remain mostly gravitationally bound, while the gas components can separate. This separation is noticeable in X-ray observations of the merging clusters by irregular morphology, increased density, cold fronts and asymmetric surface brightness [29].

The phase during which galaxy clusters have completed their collision, yet the aftermath remains clearly observable, is known as the post-merger stage. In this phase, the intracluster medium (ICM) begins to re-establish gravitational equilibrium; however, distortions induced by previous shock waves and turbulence persist [29, 42].

X-ray observations commonly reveal irregular temperature distributions, expanding gas substructures, cold fronts, disrupted metal abundance gradients, and off-center surface brightness profiles [43]. Additionally, radio observations often detect fading radio halos and peripheral radio relics (remnants of past merger shocks) of the merger, induced turbulence and particle acceleration, but these features tend to diminish as the system evolves toward symmetry [35, 44].

While the galaxy distribution may appear more relaxed compared to the merging phase, the ICM can still exhibit significant asymmetries, which may arise from residual bulk motions or external environmental effects. The post-merger phase not only offers insight into the dynamical evolution of the intracluster medium but also provides valuable constraints on large-scale structure formation and the thermal history of the universe.

### 1.1.5. Basic Properties of Galaxy Clusters & Intracluster Medium

Galaxy clusters typically consist of hundreds to thousands of galaxies. The total mass of a typical galaxy cluster ranges from $10^{14}$ to $10^{15}$ $M_{\odot}$. Due to their multicomponent structure, galaxy clusters play a critical role in tracing the large-scale structure of the universe, the distribution of matter, and cosmological evolution.

However, the galaxies themselves constitute only a small fraction of the total baryonic mass. A much more dominant component is the hot, ionized gas known as the intracluster medium (ICM), which fills the space between galaxies. This plasma, which makes up most of the ordinary matter, is found at temperatures of $10^7$–$10^8$ K and can be studied in detail through X-ray observations [45]. In addition to all these baryonic components, which account for only about 15% of the total mass of the cluster, approximately 85% consists of dark matter. Although dark matter cannot be observed directly, its existence is inferred from its gravitational effects [45]. It dominates the gravitational potential of the cluster, thereby binding together both the galaxies and the ICM, and plays a central role in determining the overall dynamics of galaxy clusters.

There are several main reasons why the ICM reaches such high temperatures. The most important of these are galaxy cluster mergers, supernova explosions, and active galactic nucleus (AGN) feedback. The most basic heating mechanism is thought to be the gas compression under the gravitational potential of the cluster.

When two or more galaxy clusters collide, the hot gases in their contents also merge and the plasma is heated even more by the shock waves and pressure that occur in this process [32]. AGN feedback is the heating of the surrounding gas by a supermassive black hole (usually located in the Brightest Cluster Galaxy - BCG) at the center of the cluster through high-energy jets and radiation [46]. Similarly, supernova explosions also contribute to the heating of the ICM by heating the surrounding gas with shocks that occur in the final stages of stars.

After the cluster is heated, it starts to lose energy over time due to continuous radiation in the X-ray band, and begins to cool. This cooling process varies according to the temperature and density of the gas. This cooling period is calculated by [47];

$$t_{cool} \equiv \frac{\frac{5}{2} n_e k T}{n_e^2 \Lambda} \; . \tag{1.1}$$

In this equation, $n_e$ represents the electron density, $T$ is the temperature, $k$ is the Boltzmann constant, and $\Lambda(T)$ denotes the cooling function, which depends on the gas temperature and metal abundance.

When we look at the Equation (1.1) we can clearly see that, high-density regions, such as the center of galaxy clusters, will cool much faster than their surroundings. Therefore, in cool-core clusters, the gas cools by losing energy near the center on short time scales, and this is supported by the observable X-ray luminosity profiles. In addition, the fact that the cooling time is also related to other parameters such as temperature and metallicity shows that this equation is an important tool for understanding the evolutionary state of galaxy clusters.

Cooling flow is a dynamic process that occurs when the hot plasma ICM at the centers of galaxy clusters rapidly loses energy through X-ray emission. Since the X-ray luminosity of the ICM is proportional to the square of its density, the luminosity increases as the density increases at the cluster centers.

The temperature of the gas in these regions is usually half or one-third of the temperature in the outer parts of the cluster. This causes the cooling period of the ICM near the center to be relatively short, less than a billion years. As the gas cools, it sinks toward the center, causing more gas to flow into the center under the pressure of the ICM above it. This continuous inflow is called the cooling flow.

If the system is in equilibrium, that is continuous cooling and inflow, then the mass deposition rate is expressed by the following equation:

$$\dot{M} = \frac{2}{5}\frac{L\mu m}{kT} \tag{1.2}$$

where $\dot{M}$ is the mass deposition rate, $L$ is the bolometric luminosity of the cooling region, $T$ is the temperature, $k$ is the Boltzmann constant, and $\mu m$ is the mean molecular mass. This equation allows us to estimate how much matter in a cluster cools and sinks to the centre per year, from the observed X-ray emission [47, 48].

## 1.2. Enrichment of Intracluster Medium

In the early universe, the lightest elements, hydrogen and helium, were present, and over time, thanks to nuclear reactions taking place in the cores of stars, these simple elements began to transform into heavier, more complex elements such as carbon, oxygen, and iron. Stars synthesize light elements into heavier elements through nuclear fusion processes throughout their life cycles, thus forming the primary source of chemical diversity in the universe. In this section, the origin of the elements observed in the universe, the mechanisms of nucleosynthesis within stars, and the fundamental physical principles underlying these processes will be discussed in detail.

### 1.2.1. Stellar Nucleosynthesis

A large portion of the heavy elements that play an important role in the chemical evolution of the universe are formed by nuclear reactions inside stars and explosions that occur during star deaths.

Type II and Type Ia supernovae play an important role during these processes and help synthesize heavy elements with the high temperatures and pressures they release.

Nuclear fusion reactions that enable the conversion of hydrogen into helium were first modeled in stars by Bethe and his colleagues in the early 20th century [49].

In low-mass stars, energy production mostly occurs through the proton-proton (p-p) chain. In this chain, two protons combine to form deuterium following;

$$\begin{aligned} \mathrm{H} + \mathrm{H} &\longrightarrow {}^{2}_{1}\mathrm{D} + e^{+} \\ {}^{2}_{1}\mathrm{D} + \mathrm{H} &\longrightarrow {}^{3}_{2}\mathrm{He}\ . \end{aligned} \tag{1.3}$$

This nucleus combines with new protons to reach the helium-4 nucleus, which can be represented as:

$${}^{3}_{2}\mathrm{He} + {}^{3}_{2}\mathrm{He} \longrightarrow {}^{4}_{2}\mathrm{He} + \mathrm{H} + \mathrm{H}\ . \tag{1.4}$$

During this process, a large amount of energy is released and approximately 26 MeV of energy is produced as a result of a hydrogen-helium cycle [50].

In high mass stars, "CNO" cycle plays an important role and it uses Carbon (C), Nitrogen (N) and Oxygen (O) as catalysts as follows;

$$\begin{aligned} {}^{12}\mathrm{C} + \mathrm{H} &\longrightarrow {}^{13}\mathrm{N} \\ {}^{13}\mathrm{N} &\longrightarrow {}^{13}\mathrm{C} + e^{+} \\ {}^{13}\mathrm{C} + \mathrm{H} &\longrightarrow {}^{14}\mathrm{N} \\ {}^{14}\mathrm{N} + \mathrm{H} &\longrightarrow {}^{15}\mathrm{O} \\ {}^{15}\mathrm{O} &\longrightarrow {}^{15}\mathrm{N} + e^{+} \\ {}^{15}\mathrm{N} + \mathrm{H} &\longrightarrow {}^{12}\mathrm{C} + {}^{4}\mathrm{He} \end{aligned} \quad . \tag{1.5}$$

The proton-proton (pp) chain is more common in smaller, sun-like stars, while the CNO cycle is more common in larger, hotter stars.

The proton-proton (pp) chain converts hydrogen into helium through nuclear fusion, while the CNO cycle also fuses hydrogen into helium but uses carbon, nitrogen, and oxygen nuclei as catalysts in the process. In this way, it creates heavier elements over time and disperses them into space, forming the chemical basis for life itself.

### 1.2.2. Non-Main Sequence Stars

On a Hertzsprung–Russell Diagram, stars are plotted based on their effective temperature versus absolute magnitudes, or simply on their colors versus luminosities. Most stars, including our Sun, fall into a neat diagonal line. These are called the "main sequence stars". They mainly burn Hydrogen. However, as stars age, they tend to evolve based on their initial masses and chemical compositions, and eventually leave the main sequence branch and start to behave peculiarly.

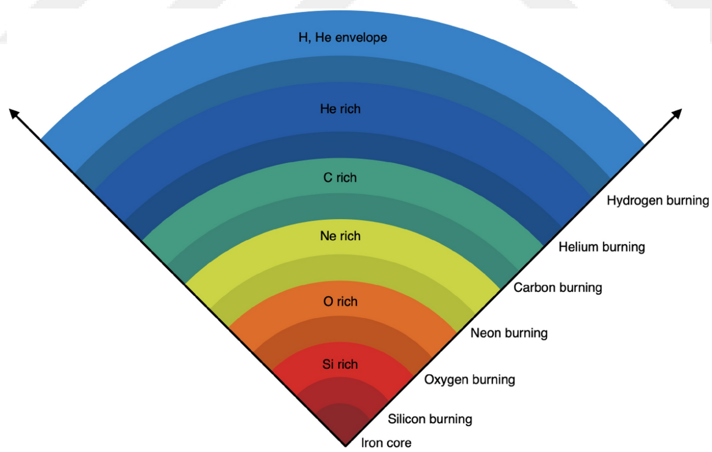


Figure 1.3. Onion-like structure of a massive star near the end of its life, before supernova. Credit: [51].

Most stars, including our Sun, are listed on the Hertzsprung–Russell Diagram according to their temperature, absolute luminosity, and color. In this diagram, the vast majority of stars on the main sequence burn hydrogen in their cores, and as they age, they evolve and show different characteristics by leaving the main sequence. The higher the mass of the evolving star, the faster this evolution will be.

After the hydrogen in the star's core is depleted, it continues to produce energy by burning elements from the inside out. This process creates a structure called onion shell inside the star Figure 1.3. The duration of these burning events is shown in Figure 1.4.

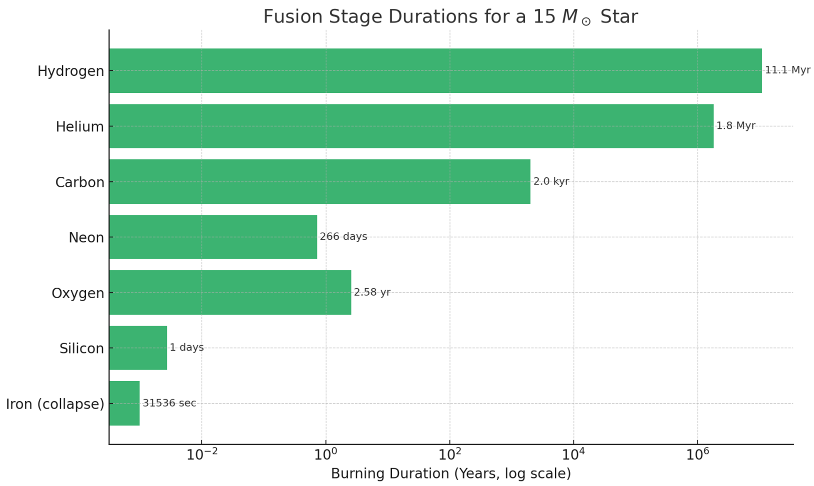


Figure 1.4. Nuclear burning timescales for a 15 $M_\odot$ star. Data adapted from [52].

When the star's core gradually begins to fill with iron, energy production ends and internal pressure decreases. Then the Chandrasekhar limit is exceeded (1.4 $M_\odot$), the core collapses and in a short time the outer layers of the star throw matter into space with a supernova explosion. With this explosion, all the heavy elements produced inside the star are dispersed into the interstellar medium and this contributes to the chemical enrichment of the universe.

### 1.2.3. Core Collapse Supernovae (SNcc)

SNccs are explosions that occur at the end of the lives of stars, which are usually 10 times more massive than the Sun. When the core of a star exceeds 1.4 solar masses (Chandrasekhar Limit), electron degeneracy pressure cannot prevent further collapse of the core, and the core rapidly collapses. During this collapse, the core temperature reaches about 100 billion Kelvin, and a large amount of gamma rays are released.

These gamma rays break up the atoms around the core into their elementary components: protons, neutrons, and electrons [53].

When the core reaches a very high density, protons capture electrons around them and turn into neutrons. This electron capture process not only produces neutrons, but also releases a large amount of electron neutrinos. Since neutrinos rarely interact with matter, they easily escape the core, carrying energy away [54]. The collapse of the star is stopped by the neutron degeneracy pressure, and the outer layers bounce back, hitting the core. This bounce creates the shock wave that initiates the explosion [55]. The neutrino emissions provide additional energy to the shock wave, causing the explosion to power up and rapidly blow away the outer layers [56].

During these supernova explosions, heavy elements, especially those heavier than iron, are produced by the rapid neutron capture process (commonly known as r-process) [57]. However, most of the material produced by the explosion is “alpha elements” such as neon (Ne), magnesium (Mg), silicon (Si) and sulfur (S), which are formed during nuclear fusion [58]. Type II supernovae, in particular, play an important role in the chemical enrichment of the intergalactic medium (ICM) [59]. Type Ib and Ic supernovae are also classified as core-collapse supernovae, but are rarer and contribute less to ICM enrichment because they lose their outer hydrogen and helium layers before the explosion [60].

### 1.2.4. Type Ia Supernovae (SNIa)

Type Ia supernovae (SNIa), unlike core-collapse supernovae (SNccs), do not occur as a result of the natural evolution of a star, but as a result of the evolution of white dwarf stars in binary star systems. When a white dwarf begins to accrete matter from a nearby star, it explodes and completely disappears as its mass approaches the Chandrasekhar Limit. These supernovae occur as a result of a thermonuclear chain reaction that begins with the carbon fusion of the white dwarf star, leaving no remnant at the end of the explosion [61].

White dwarfs can be imagined as dormant stellar cores made mostly of carbon, incapable of expanding or contracting to regulate their temperature. If one were to gradually collect more material until it was hot enough to start fusing the accreted material, we would end up with a regular nova. However, if the mass of the white dwarf begins to approach the Chandrasekhar Limit and its temperature reaches the point of carbon fusion, a cataclysmic chain reaction will occur [62].

The kinetic energy released during an SNIa explosion is around $10^{44}$ J, which is enough to completely disintegrate the white dwarf [63]. Indeed, there is no compact stellar remnant left after an SNIa explosion. Moreover, all SNIa have similar absolute luminosity profiles, with a luminosity peak and a brightness decay. Although their apparent luminosities are not the same, a correction that relates an SNIa's peak luminosity to its decay rate can be applied to calculate its absolute luminosity. This makes SNIa invaluable tools for studying the expansion of the Universe, as they can be found anywhere from the early Universe to the present day [64, 65].

A substantial portion of the Universe's calcium (Ca) and argon (Ar), alongside iron-peak elements such as chromium (Cr), manganese (Mn), iron (Fe), cobalt (Co), and nickel (Ni), is generated by Type Ia supernova explosions. Unlike Type Ib and Ic supernovae, the elemental output from Type Ia supernovae leans significantly towards heavier elements, notably iron (Fe) [66].

These stellar explosions are prolific producers of iron-peak elements, substantially contributing to the observed iron (Fe) abundance throughout the cosmos. However, elements heavier than those typically formed in supernovae, like gold (Au) and uranium (U), are primarily synthesized during rare and exotic events, such as neutron star mergers. Consequently, these heavier elements are far less prevalent in the natural world [67].

In essence, while Type Ia supernovae are crucial for the creation of iron (Fe) and related elements, the synthesis of even heavier elements is relegated to much less frequent cosmic events, resulting in their comparatively lower abundance [67].

## 1.3. Emission Mechanisms

Galaxy clusters are composed not only of galaxies and dark matter, but also of a large amount of hot, diffuse gas known as the intracluster medium (ICM). This medium reaches temperatures of tens of millions of Kelvin, causing most atoms, especially hydrogen and helium, to become fully ionized. Although ICM is extremely low in density, its volume is so large that collisions between particles (mainly electrons and ions) still occur frequently enough to establish thermodynamic properties [45].

Under such conditions, the ICM can be described as being in Collisional Ionization Equilibrium (CIE). In this state, the rate at which atoms lose electrons through ionizing collisions is balanced by the rate at which ions recombine with electrons. This balance means that ions are typically found in their ground state. However, collisions with energetic electrons can excite these ions, and as they return to lower energy levels, they emit X-ray photons at specific energies, producing what we observe as line emission from metals (e.g., Fe, Si, S lines) [68].

In addition to these line emissions, the ICM also emits continuous X-ray radiation primarily through bremsstrahlung (free-free emission), a process where fast-moving electrons are deflected by the Coulomb fields of ions, resulting in a broad X-ray spectrum. Together, these emission processes allow us to determine key physical properties of the ICM—such as temperature, density, and elemental abundances—through X-ray spectral analysis [69].

### 1.3.1. Continuum Emission

When free-flowing electrons inside a hot plasma collide with or pass nearby an ion, they get deflected and lose kinetic energy. This lost energy is emitted as a high-energy photon. This process is called the bremsstrahlung (braking) radiation. It is also referred to as “free-free radiation” since it involves unbound, free ions interacting with each other. Bremsstrahlung is the dominant radiative process in the ICM, and it determines the overall shape of the X-ray spectra coming from the ICM.

The emissivity is defined as the total energy emitted per unit time, per unit volume, and per unit frequency. For a plasma with temperature $T_g$, and ion and electron number densities $n_i$ and $n_e$, the total free-free emissivity $\epsilon_\nu^{ff}$ produced by an ion with charge $Z$ at frequency $\nu$ is expressed as [45]:

$$\epsilon_\nu^{ff} = \underbrace{\frac{2^5 \pi e^6}{3 m_e c^3} \left( \frac{2\pi}{3 m_e k} \right)^{1/2}}_{\text{physical constants}} Z^2 n_e n_i \underbrace{g_{ff}(Z, T_g, \nu)}_{\text{Gaunt factor}} T_g^{-1/2} \exp\left( -\frac{h\nu}{kT_g} \right) \tag{1.6}$$

where the function $g_{ff}$ accounts for quantum mechanical corrections and the influence of distant electron-ion encounters. Known as the Gaunt Factor, it is a dimensionless quantity that modifies the classical bremsstrahlung emissivity and varies slowly with both temperature and frequency [70].

Since the intracluster medium (ICM) is optically thin, photons emitted from this medium do not re-interact with the plasma and are ejected out. This shows that the ICM is cooled by thermal bremsstrahlung radiation. This is more common in cool-core galaxies because in these types of galaxy clusters the core emits more x-rays and is at a lower temperature than its surroundings.

### 1.3.2. Line Emission

The intracluster medium (ICM) is largely determined in the X-ray spectrum by bremsstrahlung (braking) radiation. The free electrons inside the ICM, which is at high temperatures, have high speeds and change direction as they pass through the electric field inside the cluster. During this time, the electrons accelerate and emit electromagnetic radiation called bremsstrahlung (braking radiation).

In the X-ray spectra, it is also possible to observe distinct line emissions from metal ions at certain frequencies.

These line emissions are due to photons emitted during the excitation of electrons that remain bound to the atoms and their subsequent transition to lower energy levels. For this reason, this type of radiation is called ”bound-bound radiation”.

The X-ray emissivity of the collisionally stimulated line emission is given by [45] as:

$$\int \epsilon_\nu^{line} d\nu = n\left(X^i\right) n_e \frac{h^3 \nu \Omega(T_g) B}{4\omega_{gs}(X^i)} \left[\frac{2}{\pi^3 m_e^3 k T_g}\right]^{1/2} \exp\left(-\Delta E/kT_g\right) \tag{1.7}$$

where $n(X^i)$ is the density of the ion, $\omega_{gs}$ is the statistical weight of the ground state, $\Omega$ is the collision intensity depending on the temperature, $B$ is the probability of transition to a lower state, and $\Delta E$ is the excitation energy.

Equation (1.7) gives the total X-ray emissivity of the line emission resulting from the excitation of a particular type of ion $(X^i)$ by collision with electrons in a hot and ionized plasma. This emissivity depends on the ion and electron densities, the temperature of the gas, and the atomic properties of the transition. In particular, due to the presence of the excitation energy $\Delta E$, this emission decays exponentially with temperature. The equation clearly shows the sensitivity of the line emissions to the physical conditions of the plasma.

## 1.4. Chemical Abundance Measurements

Studying the chemical abundances in the intracluster medium (ICM) provides important information about the enrichment history of galaxy clusters. As seen in Figure 1.5, the soft X-ray band between 0.1 and 10 keV in the spectrum obtained with XMM-Newton contains prominent emission lines from elements Carbon to Nickel [71]. These lines originate from electronic transitions in heavy ions and are of great importance in investigating the cumulative yields of different types of supernovae (SNIa and SNcc) that contribute to the metal content of the ICM.

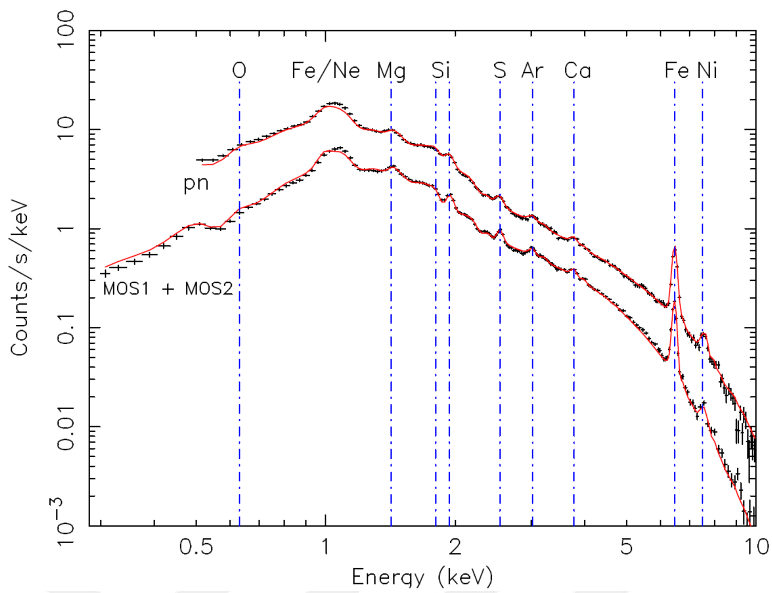


Figure 1.5. Spectra of the core region of the cluster 2A 0335+096 observed with XMM-Newton's PN, MOS1 and MOS2 cameras. The elemental line values are indicated by the blue dotted lines. Credit: [71].

When modeling XMM-Newton, it is important to take into account instrumental background lines. Table 1.1 lists the most prominent fluorescence instrumental lines in XMM-Newton's MOS and PN detectors. These lines arise from the interactions of high-energy particles with the detector materials. Since these lines can overlap with emission lines, they should be carefully modeled and removed during spectral analysis for reliable modeling.

### 1.4.1. X-ray Spectral Analysis

The X-ray spectra of hot plasmas provide critical insights into their physical conditions and chemical composition. In galaxy clusters, the intracluster medium (ICM) which is a diffuse, ionized gas at temperatures of tens of millions of Kelvin, emits strongly in the X-ray band. This emission primarily arises from two mechanisms: thermal bremsstrahlung (free-free radiation), resulting from collisions between high-energy electrons and ions, and discrete line emission produced by heavy elements present in the plasma.

Table 1.1. Fluorescent instrumental lines produced by hard particles in XMM-Newton detectors.

| **MOS** | | **PN** | |
|---|---|---|---|
| **Energy (keV)** | **Line** | **Energy (keV)** | **Line** |
| 1.49 | Al K$\alpha$ | 1.48 | Al K$\alpha$ |
| 1.75 | Si K$\alpha$ | 4.51 | Ti K$\alpha$ |
| 5.41 | Cr K$\alpha$ | 5.42 | Cr K$\alpha$ |
| 5.90 | Mn K$\alpha$ | 6.35 | Fe K$\alpha$ |
| 6.40 | Fe K$\alpha$ | 7.47 | Ni K$\alpha$ |
| 7.48 | Co K$\alpha$ | 8.04 | Cu K$\alpha$ |
| 8.64 | Zn K$\alpha$ | 8.60 | Zn K$\alpha$ |
| 9.71 | Au L$\alpha$ | 8.90 | Cu K$\beta$ |
| | | 9.57 | Zn K$\beta$ |

*Notes.* Centroid energies adapted from [72] and [73], and adjusted using our best-fit model (pn + MOS Si K).

The ICM is composed of highly ionized gas with temperatures ranging from a few million to over $10^8$ K. At these temperatures, the dominant mechanisms of X-ray emission are as follows:

- Continuum emission from thermal bremsstrahlung (free-free radiation), which results from collisions between electrons and ions.
- Line emission from heavier elements such as iron, silicon and sulfur, arising from bound-bound transitions in partially ionized ions [2].

The shape of the X-ray spectrum is directly linked to plasma temperature. Low-temperature plasmas produce softer X-rays with prominent line features, while high-temperature plasmas emit harder, high-energy X-rays and show reduced line emission due to full ionization of heavy elements [4]. To interpret these spectra, we employ plasma emission models that simulate both continuum and line components.

The two principal models used in this work are:

- APEC: Provides estimates of the global plasma temperature and metallicity.
- VAPEC: An extension of apec that allows individual elemental abundances (e.g., Ne, Mg, Si, S, Ca, Fe) to vary independently, enabling more detailed studies of chemical enrichment [74].

These models are implemented in the XSPEC spectral fitting software [75], where observed spectra are fitted to determine the best-fit physical parameters. Uncertainties in parameters are derived through statistical error analysis, typically quoted at the 90% confidence level.

Understanding the thermal and chemical properties of the intracluster medium (ICM) offers valuable insights into the formation and dynamical evolution of galaxy clusters, the impact of feedback processes such as AGN activity and supernova enrichment, and the spatial distribution and origin of metals—whether produced by Type Ia or core-collapse supernovae. These spectral diagnostics play a crucial role in tracing the baryonic and chemical evolution of the universe on cosmological scales.

## 1.5. XMM-Newton Observatory

The XMM-Newton (X-ray Multi-Mirror Mission), developed and operated by the European Space Agency (ESA), was launched in December 1999 with the goal of observing cosmic X-ray sources with high sensitivity. Together with NASA's Chandra X-ray Observatory, launched in July 1999, XMM-Newton opened a new era in X-ray astronomy. While Chandra excels in spatial resolution, XMM-Newton's large effective area allows it to collect many photons efficiently, making it ideal for studying extended sources such as galaxy clusters and examining their temperature and chemical composition in detail [76, 77].

Figure 1.6. Artist's impression of XMM-Newton operating in space. Credit: [78]

Thanks to its three X-ray telescopes and advanced detectors, XMM-Newton has been instrumental in research on topics ranging from black holes to galaxy clusters. It remains fully operational and continues to produce high-impact scientific results.

### 1.5.1. Spacecraft

XMM-Newton follows a highly elliptical orbit around Earth, which allows it to spend long periods away from Earth's radiation belts. This orbit was initially designed with an apogee of about 115,000 km and a perigee of around 6,000 km. As of May 2024, these values have shifted to approximately 95,500 km and 25,600 km, respectively [77].

The spacecraft has a total mass of around 3.8 tons and a length of about 10 meters. It is composed of four main parts:

- Focal Plane Assembly (FPA): Houses the EPIC (PN and MOS) detectors and the two RGS cameras.
- Mirror Support Platform (MSP): Carries the X-ray mirror modules, Optical Monitor (OM), and star trackers.
- Telescope Tube: A long carbon-fiber structure that connects the mirrors to the detectors.
- Service Module (SVM): Contains subsystems for power, communication, thermal

control, and two S-band antennas.

XMM-Newton does not store data onboard. Instead, all data are transmitted in real time to ESA's ground stations located in Australia, French Guiana, Chile, and Spain [77].

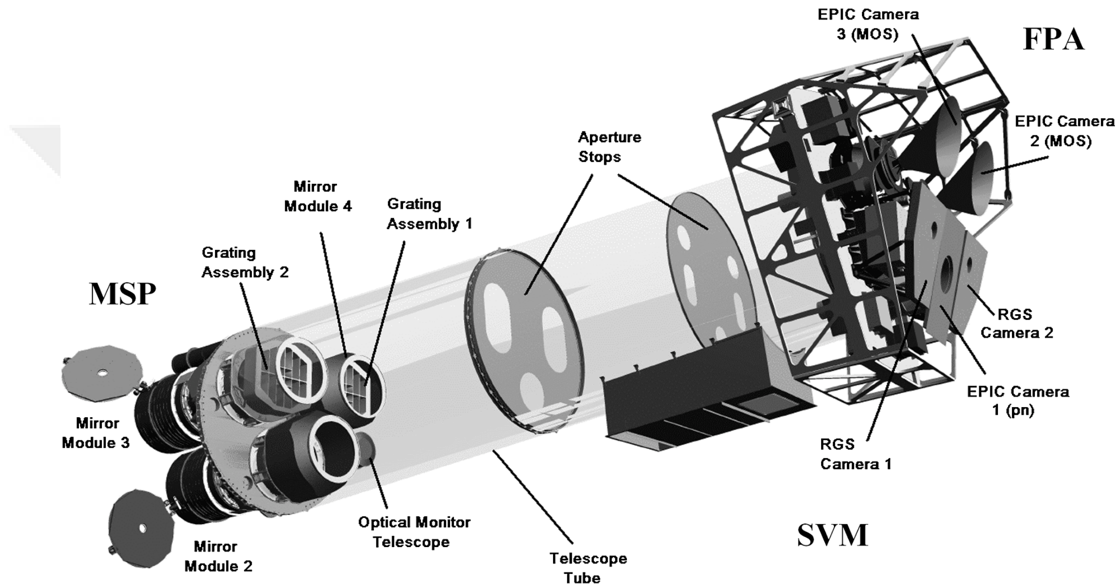


Figure 1.7. Schematic of XMM-Newton showing key spacecraft components. Credit: [77]

### 1.5.2. Telescopes

XMM-Newton is equipped with three identical Wolter-I X-ray telescopes. Each consists of 58 nested, gold-coated nickel mirrors that focus incoming X-rays by grazing incidence. The largest mirror has a diameter of about 70 cm, and the focal length is 7.5 meters [76].

Key components of each telescope include:

- Mirror Assembly Door: Protected the optics before launch and was opened once the mission began.

- Entrance and X-ray Baffles: Block unwanted visible and off-axis X-ray light.
- Mirror Module: Focuses X-ray photons.

- Electron Deflector: Uses a magnetic field to deflect soft electrons that could interfere with observations.
- Reflection Grating Assembly (RGA): Diverts part of the X-ray beam to the RGS detectors for high-resolution spectroscopy [77].

### 1.5.3. Instruments

The scientific payload includes six instruments:

- 3 EPIC cameras: One PN and two MOS detectors for X-ray imaging and spectroscopy.
- 2 RGS units: For high-resolution X-ray spectroscopy.
- 1 Optical Monitor (OM): For ultraviolet and optical observations.

The MOS cameras each contain 7 CCDs with 600 $\times$ 600 pixels of 40-micron size. They operate in different readout modes to accommodate varying brightness levels, with readout times ranging from 2.6 seconds (full-frame) to 0.3 seconds (small window) [79].

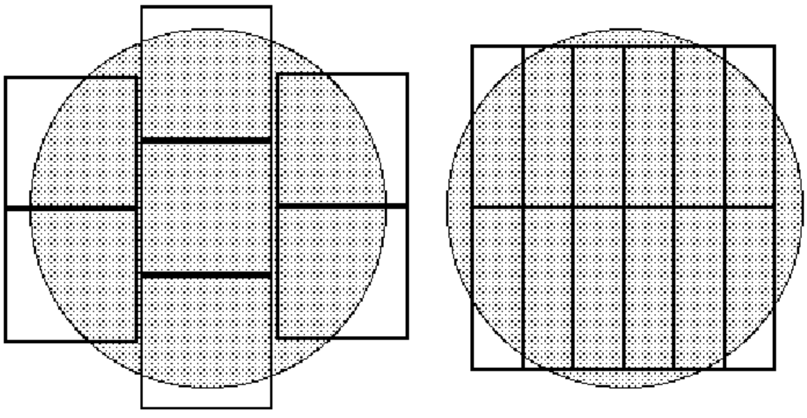

Figure 1.8. CCD layout for EPIC MOS (left) and PN (right) cameras. Credit: [80].

The PN detector uses 12 CCDs, each $3 \times 1$ cm, with $200 \times 64$ pixels. It has a fast readout cycle of 73.3 ms, of which 4.6 ms is for reading and the rest is for photon collection. About 6% of detected events occur during readout (known as out-of-time events) and are corrected in data processing [81].

Both MOS and PN cameras are sensitive to X-rays in the 0.15–15 keV range and cover a field of view of about 30 arcminutes [77].

### 1.5.4. Calibration

Accurate X-ray analysis requires well-calibrated instrument responses. XMM-Newton's calibration is maintained using the Current Calibration Files (CCF) distributed by ESA [82]. These files are regularly updated to account for detector aging, gain changes, and other instrumental effects.

Key calibration components include:

- Effective Area: Describes the sensitivity of the mirrors and detectors over energy.
- Response Matrix File (RMF): Maps incoming photon energies to the detector's output.
- Ancillary Response File (ARF): Includes telescope area and detector efficiency.
- Gain and CTI Corrections: Account for temporal changes and charge transfer inefficiency in CCDs [83].

For extended sources like galaxy clusters, ESA provides the Extended Source Analysis Software (ESAS) package. ESAS enables filtering, background modeling, and particle contamination correction, ensuring the scientific integrity of the final products [72].

## 1.6. Chandra X-ray Observatory

The *Chandra X-ray Observatory*, developed by NASA and launched on July 23, 1999, is an advanced space telescope designed to observe high-energy X-rays emitted by hot plasmas and energetic astrophysical phenomena. Named after Nobel Prize-winning physicist Subrahmanyan Chandrasekhar, Chandra is one of the most powerful X-ray telescopes in orbit, offering the highest angular resolution ever achieved in X-ray astronomy.

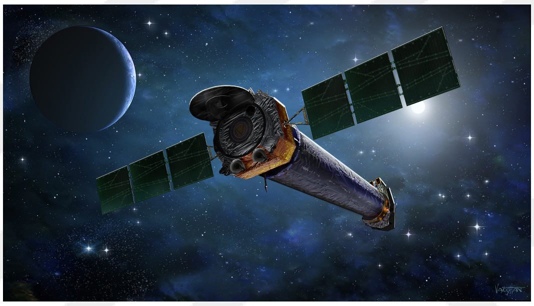

Figure 1.9. Artistic illustration of the Chandra X-ray Observatory in space. This visual highlights Chandra's highly elliptical orbit around Earth and commemorates its 20 years of contributions to X-ray astronomy. Credit: [84]

Chandra has played a crucial role in the observation of extreme cosmic environments such as galaxy clusters, supernova remnants, black holes, and neutron stars. Its high-resolution images have enabled detailed studies of temperature, density, motion, and chemical composition throughout the universe [85], [86].

### 1.6.1. Spacecraft and Orbit

Chandra follows a highly elliptical orbit around Earth, designed to keep it well above the planet's radiation belts for most of its orbital period. This orbit allows uninterrupted observations for up to 55 hours per 64-hour orbit, which is particularly advantageous for long-exposure X-ray studies [87].

The spacecraft weighs approximately 4.8 tons and is composed of four main sections:

- Science Instrument Module (SIM): Houses the mirrors and detectors.
- Telescope Structure: Supports the mounting and alignment of the mirror assemblies.
- Spacecraft Module: Contains power, thermal control, communication, and data systems.
- Integrated Propulsion System: Used for orbit correction and spacecraft maneuvering.

### 1.6.2. Telescope and Mirror System

Chandra's telescope system uses a Wolter-I design, which focuses X-rays through grazing incidence reflection. The observatory contains four nested mirror pairs, providing an unprecedented angular resolution of 0.1 arcseconds. This resolution is about ten times sharper than that of the Hubble Space Telescope [85].

Such high precision enables detailed investigation of black hole environments, dense gas in cluster cores, and sharp features like shock fronts.

### 1.6.3. Scientific Instruments

The observatory is equipped with four main scientific instruments:

- Advanced CCD Imaging Spectrometer (ACIS): Performs both imaging and spectral analysis by measuring the position and energy of incoming X-ray photons with high accuracy.
- High Resolution Camera (HRC): Provides excellent time resolution, ideal for detecting fast phenomena such as bursts and pulsations.
- High Energy Transmission Grating Spectrometer (HETGS) and Low Energy Transmission Grating Spectrometer (LETGS): Disperse X-rays to obtain high-resolution spectra across different energy ranges.

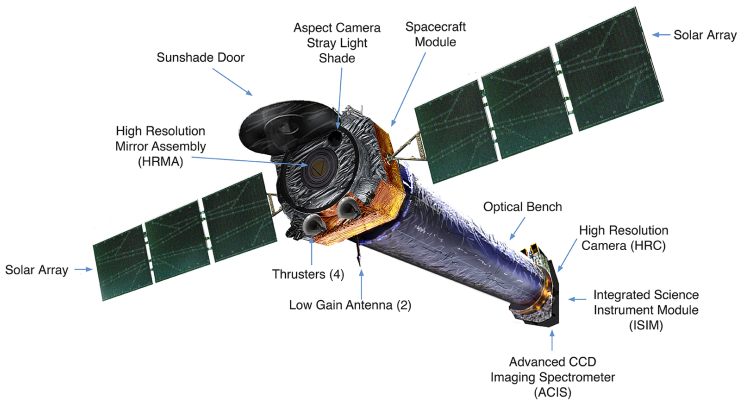


Figure 1.10. Labeled Chandra X-ray Observatory schematic, showing the main structural components including the scientific instruments, mirror assembly, spacecraft module, and propulsion system. Credit: [88]

Together, these instruments allow Chandra to observe in a wide energy range of approximately 0.1–10 keV with remarkable sensitivity [86].

### 1.6.4. Calibration and Data Processing

The accuracy of Chandra's scientific results is ensured through rigorous calibration of its mirrors and detectors. Instrument responses (including effective area and energy resolution) are continuously monitored and updated. Data analysis is performed using NASA's *Chandra Interactive Analysis of Observations (CIAO)* software suite [89].

Each observation includes:

- Response Matrix Files (RMFs): Define the mapping from photon energy to detector output.
- Ancillary Response Files (ARFs): Contain effective area and energy-dependent efficiency information.

Detector responses can change due to long-term effects, such as radiation damage. These calibration files are essential for interpreting the observed spectra accurately.

# 2. ABELL 2384 GALAXY CLUSTER

Abell 2384 is a relatively nearby galaxy cluster located at a redshift of $z = 0.0943$, placing it at a comoving radial distance of approximately 432 Mpc. It is classified as richness class 1 in the Abell catalog, indicating a moderate galaxy population within the cluster, and falls under the Bautz–Morgan type II–III, suggesting the absence of a single dominant brightest cluster galaxy (BCG) [90]. Unlike relaxed, spherically symmetric systems, A2384 displays a highly disturbed morphology with a pronounced elongation along the north–south axis. This elongation is consistent with a bimodal structure, where the cluster is composed of two distinct subcomponents: A2384(N) to the north and A2384(S) to the south.

Figure 2.1. Composite image combining X-ray, optical, and radio observations of Abell 2384. Image credit: NASA/CXC/SAO/V. Parekh et al. [91].

These two subclusters are connected by a prominent filament of hot gas, clearly observed in X-ray images obtained with both Chandra and XMM-Newton. This interconnecting structure extends over a projected length of approximately 700–1100 kpc and exhibits enhanced temperature and density relative to the surrounding intracluster medium (ICM), consistent with the remnant of a major post-merger event [7, 8].

The observed continuity and brightness of the filamentary X-ray emission strongly suggest that it is not a line-of-sight superposition, but rather a genuine physical feature produced by the interaction and dynamical mixing of the two subclusters.

Unlike many other clusters that host a single central dominant galaxy, A2384 contains two BCGs associated with its respective subclusters. A2384(N) is centered on LEDA 190740, while A2384(S) is located around LEDA 67523. Interestingly, both BCGs are offset from their corresponding X-ray peaks by ∼10–15 arcseconds for the northern component and by nearly 40 arcseconds for the southern one. These offsets are commonly interpreted as signatures of dynamical disturbance and are frequently observed in post-merger systems where the collision has decoupled the collisionless galaxies and dark matter from the collisional hot gas component [7].

Spectroscopic studies further support the merger scenario. Both subclusters exhibit high galaxy velocity dispersions on the order of ∼1000 km $s^{-1}$, indicative of deep gravitational potential wells and turbulent dynamical states. Additionally, the radial velocity of the BCG in A2384(N) shows a significant offset of approximately 600 km $s^{-1}$ from the mean velocity of its surrounding galaxies [38]. These findings point toward a scenario in which the two subclusters underwent a major collision roughly 1–1.5 Gyr ago, and the system is now observed in a post-merger relaxation phase.

A particularly striking feature within the X-ray bridge is a morphological distortion located approximately 800 kpc from the northern X-ray peak [90]. This distortion coincides with the position of an FR I type radio galaxy, LEDA 851827, which is a confirmed member of A2384(S). The galaxy exhibits two radio lobes extending in the northeast–southwest direction. The northeastern lobe physically interacts with the X-ray-emitting gas, displacing the hot plasma eastward by nearly 400 kpc and producing a noticeable bend in the filament's morphology.

Such large-scale deflections caused by a radio lobe are extremely rare and mark one of the first direct observational cases of AGN–ICM interaction on this scale.

In previous study, to quantify the impact, a surface brightness (SB) profile was extracted along the direction of the northeast lobe using both Chandra and XMM-Newton data. The resulting profile revealed a distinct discontinuity in the X-ray emission, well-described by a broken power-law model. This discontinuity is interpreted as a weak shock front, likely induced by the expansion of the radio lobe into the surrounding ICM. The derived density jump corresponds to a Mach number of $\mathcal{M}_\delta = 1.09 \pm 0.06$, and independent temperature measurements yield a temperature-based Mach number of $\mathcal{M}_T = 1.25 \pm 0.035$ [90].

These results strongly suggest that LEDA 851827 is actively perturbing the ICM, altering both the thermal and morphological properties of the bridge region. This makes A2384 a compelling case study for AGN feedback mechanisms outside of traditional cool-core environments.

In addition to the AGN-related structures, a recent MeerKAT observation revealed two new diffuse radio features. The first is a large radio relic discovered at the southern periphery of A2384(S), previously misidentified as the southern lobe of the FR I galaxy in GMRT data [8]. This relic, measuring approximately $824 \times 264$ kpc$^2$, is elongated perpendicular to the merger axis and exhibits a steep spectral index of $\alpha \approx -2.5$, suggesting reacceleration of fossil electrons from past AGN activity. The second feature is a faint, diffuse radio ridge of $\sim 182 \times 129$ kpc$^2$, located within the X-ray bridge. This ridge shows no optical counterpart and may represent a new class of merger-induced radio emission associated with turbulence in the intra-cluster medium [8].

Thermodynamic maps constructed from XMM-Newton observations further confirm elevated entropy and temperature in the X-ray bridge, particularly near the interaction site of the northeastern radio lobe. Additionally, metallicity maps derived from Chandra data show central enrichment levels up to $Z \sim 0.5\, Z_\odot$, gradually declining with radius [90]. These findings reinforce the significance of AGN–ICM interplay in shaping the dynamical and thermodynamic state of the cluster core.

Taken together, the observed features (such as the bimodal structure, disturbed gas bridge, AGN-induced shock, relic and ridge emission ) establish Abell 2384 as a rare and valuable system for probing post-merger dynamics, AGN feedback, and diffuse radio phenomena in galaxy clusters.

# 3. OBSERVATIONS AND DATA REDUCTION OF A2384

## 3.1. Data Analysis Overview

After completion of the observations by XMM-Newton and Chandra, the respective datasets become publicly available through the XMM Science Archive (XSA) [39] and the Chandra Data Archive (CDA), accessible via the ChaSeR interface [92]. The standard data analysis workflow begins with downloading the relevant Observation Data Files (ODFs) or event data products. For XMM-Newton, the data is processed using the Science Analysis System (SAS) to produce cleaned and calibrated event files. Similarly, Chandra data are reprocessed with the Chandra Interactive Analysis of Observations (CIAO) software, where the `chandra_repro` script ensures up-to-date calibration and creates level 2 event files.

In both cases, X-ray images are generated from the cleaned datasets and examined using the visualization tool SAOImage DS9. Source and background regions of interest are defined manually within DS9, and spectra are extracted using the appropriate tasks—SAS routines for XMM-Newton and `specextract` in CIAO for Chandra. These tasks also generate the corresponding response files necessary for spectral modeling. The extracted spectra are then analyzed in XSPEC software, where astrophysical models are fitted to determine key physical properties such as plasma temperature, metallicity, and hydrogen column density.

## 3.2. Observational Data

As of April 2025, the A2384 galaxy cluster has been observed once by each of the *XMM-Newton* and *Chandra* satellites. The XMM-Newton observation (ObsID: 0201902701) was carried out on October 28, 2004, with a nominal exposure time of 26 ks. However, after filtering out periods of high background flaring due to soft proton contamination, the effective exposure was reduced to 19.4 ks.

The Chandra observation (ObsID: 4202) was conducted earlier on November 18, 2002, with a nominal exposure of 31.4 ks, from which 31.2 ks remained usable after standard background cleaning procedures. Both datasets were downloaded from the XMM Science Archive (XSA) and the Chandra Data Archive (CDA), respectively, and were processed using the latest calibration pipelines for each mission.

Table 3.1. Observational information of the A2384 galaxy cluster from *XMM-Newton* and *Chandra* satellites.

| **Satellite** | **Obs. ID** | **Observation Date** | **Duration (used)[ks]** |
|---|---|---|---|
| XMM-Newton | 0201902701 | 2004-10-28 | 26.0 (19.4) |
| Chandra | 4202 | 2002-11-18 | 31.4 (31.2) |

## 3.3. Data Reduction

### 3.3.1. XMM-Newton Data Reduction

The data reduction procedures presented in this section are based on the guidelines provided in the XMM-ESAS Cookbook [83]. The analysis was carried out using SAS version 21.0.0 and XSPEC version 12.13.1.

After downloading the observation data, the relevant calibration files must be retrieved. This can be done by entering the start and end dates of the observation on the Current Calibration Files (CCF) webpage [82]. However, in this study, we opted to download the full calibration database from ESA servers, allowing SAS to automatically select the appropriate calibration files using the metadata included in the observation files.

Once the files are in place, the paths to the observation data and calibration files are set using the `SAS_ODF` and `SAS_CCF` environment variables.

The calibration index is then generated by running the `cifbuild` task, which matches the observation dates with the relevant calibration files and produces a file named `ccf.cif`.

After updating the calibration path to point to this index file, the task `odfingest` is executed. This step produces a summary file containing both calibration and instrument information, which becomes the reference for the rest of the reduction process.

The main data reduction begins with `emchain` and `epchain`, which generate calibrated event files for the MOS and PN detectors, respectively. The `emanom` task is used to identify malfunctioning CCDs.

The soft proton flares are then filtered using the `espfilt` task, which identifies and excludes time intervals affected by elevated background levels. This step produces cleaned event files suitable for reliable spectral and imaging analysis, and the generated files are used in subsequent steps.

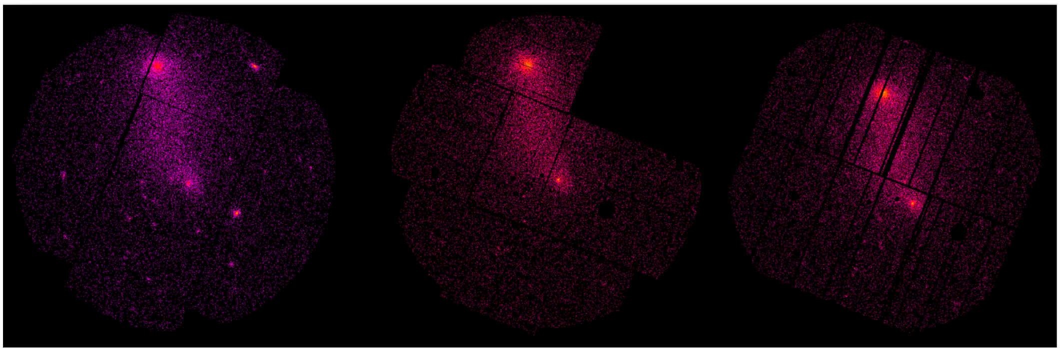

Figure 3.1. EPIC images of A2384 obtained in the 0.4–7.2 keV energy band are shown from left to right: MOS1, MOS2, and PN. Gaps caused by missing CCDs in the MOS2 detector are clearly visible.

The *cheese* command in the SAS software package is widely used for detecting and masking point sources in XMM-Newton data.

This command masks the image and ensures that these regions are excluded during the `mosspectra` and `pnspectra` tasks. However, in this study, the *wavdetect* algorithm in Chandra Interactive Analysis of Observations (CIAO) software was preferred to achieve more accurate point source extraction which is one of the most crucial steps before spectral analysis. Although the X-ray background can be modeled during the analysis or subtracted from selected source-free regions, point-like objects such as galaxies, supernova remnants, or AGNs are preferred to be removed beforehand. This ensures better spectral modeling and avoids misleading contributions.

The `wavdetect` algorithm was used to identify and remove point sources from the XMM-Newton observations. Since `wavdetect` was originally developed for Chandra data [93], applying it to MOS1, MOS2, and PN data requires both a calibrated image and a corresponding exposure map (Figure 3.2). In our study, point source detection was performed separately for each camera, and the resulting region files were merged into a single source list. These regions were visually checked for accuracy and manually excluded during spectral extraction.

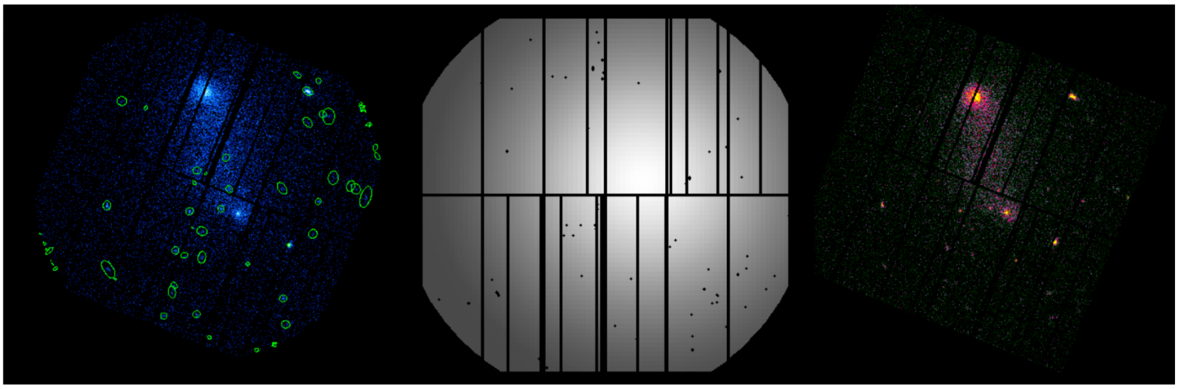

Figure 3.2. Left: Point sources detected using *wavdetect* (marked with green circles) overlaid on the PN image; Center: the corresponding PN exposure map; and Right: the raw PN image data.

To model the background, a region located far from the observed source areas and characterized by minimal X-ray emission was selected (Figure 3.3).

This region was chosen to represent typical background components, including the cosmic X-ray background (CXB), particle-induced background, and other diffuse emissions. For this background region, a separate spectral file (.pi) was created, and the corresponding Ancillary Response File (ARF) and Redistribution Matrix File (RMF) were generated using the `arfgen` and `rmfgen` tasks, respectively. By incorporating this background spectrum into the modeling of the scientific regions, more accurate and reliable results were achieved.

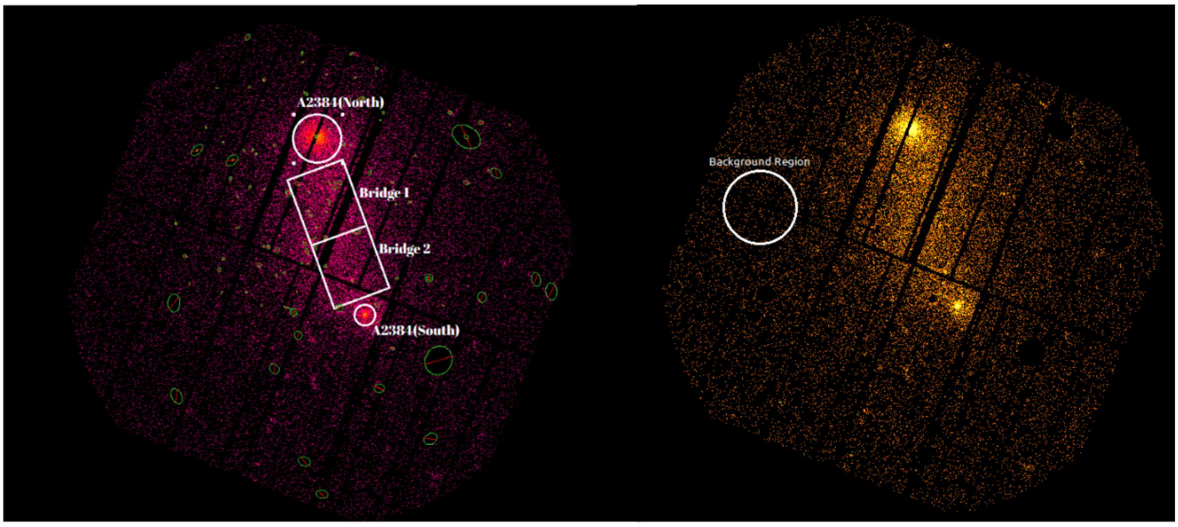


Figure 3.3. Left: White regions show A2384 (North), Bridge 1, Bridge 2, and A2384 (South) used for spectral analysis on the 0.4–7.2.keV PN image. Green marked are point sources detected by *wavdetect* and excluded. Right: The white circle indicates the background region in a source-free area, used to extract the background spectrum and create ARF/RMF files.

Next, we extracted the spectra and corresponding images for each of the four regions using the *mosspectra* and *pnspectra* tasks, within the 0.4-7.2 keV energy band. For each region, a spectrum file (.pi), Redistribution Matrix File (RMF), and Ancillary Response File (ARF) were produced automatically using the *rmfgen* and *arfgen* tools (Figure 3.4) .

Before performing spectral fitting in XSPEC, we grouped and binned the spectral files. Binning reduces noise and computational load by combining adjacent energy channels. We applied optimal binning using the *ftgrouppha* tool with the setting *grouptype=opt*, as recommended by Kaastra [94].

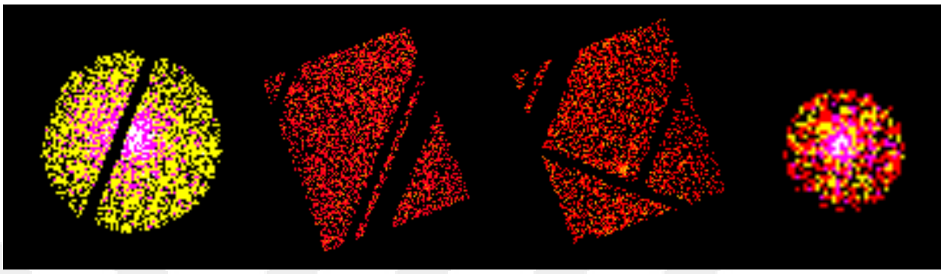

Figure 3.4. From left to right, selected regions in the PN camera: A2384 (North), Bridge 1, Bridge 2, and A2384 (South).

### 3.3.2. Chandra Data Reduction

The data reduction steps for Chandra observations were carried out using CIAO version 4.16, following the standard procedures outlined in the CIAO Science Threads provided by the Chandra X-ray Center (CXC) [89]. All necessary data products were retrieved from the Chandra Data Archive (CDA).

*Chandra* data were reprocessed using CIAO (version 4.16) and the `chandra_repro` script. Spectra and response files were extracted using the `specextract` task. Background was taken from regions on the same ACIS-S chip but away from cluster emission. Calibration files were based on CALDB version 4.9.6 or later.

Once the data was downloaded, the entire dataset was reprocessed using the `chandra_repro` script, which applies the latest calibration files and generates new level 2 event files suitable for scientific analysis. These reprocessed files were then examined using SAOImage DS9 to define appropriate source and background extraction regions (Figure 3.5).

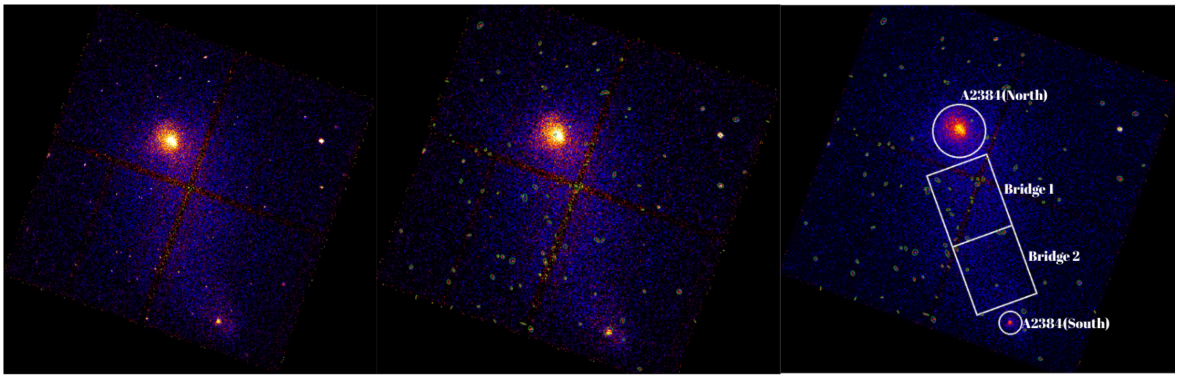


Figure 3.5. Chandra ACIS-I images of Abell 2384 in the 0.5–7. keV energy band. Left: Raw X-ray image. Center: Image with detected point sources. Right: Same image with labeled spectral extraction regions: A2384 (North), Bridge 1, Bridge 2, and A2384 (South).

The spatial distribution of X-ray events in each spectral region is shown in Figure 3.6. Spectral products were generated using the CIAO task `specextract`, which also creates the necessary response matrix (RMF) and auxiliary response (ARF) files for each region. Background subtraction was handled automatically as part of this task, using the selected background region.

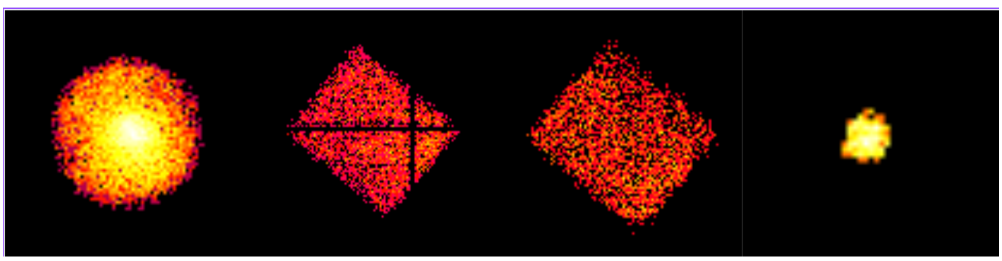

Figure 3.6. ACIS detector images of the four selected spectral regions in the 0.5-7. keV energy band. From left to right: A2384 (North), Bridge 1, Bridge 2, and A2384 (South). These images show the spatial distribution of X-ray events extracted from the Chandra ACIS-I observation.

Before spectral modeling, the extracted spectra were grouped to ensure a minimum number of counts per bin to enable the use of $\chi^2$ statistics. Spectral analysis and fitting were performed in XSPEC (version 12.13.1), using appropriate astrophysical models to derive parameters such as plasma temperature, metallicity, and hydrogen column density.

## 3.4. Spectral Modeling

To investigate the thermal and chemical properties of the intracluster medium (ICM) in A2384, spatially resolved X-ray spectral analysis was performed using data from both *XMM-Newton* and *Chandra* observations. Spectra were extracted from several regions of interest, determined based on the morphology of the X-ray surface brightness and prior thermodynamic structure maps. Each region was modeled independently using XSPEC (version 12.13.1), applying two plasma emission models: `phabs*apec` and `phabs*vapec`.

### 3.4.1. Model Descriptions

The primary model applied to all regions was the absorbed single-temperature model `phabs*apec`, which is expressed mathematically as

$$F(E) = e^{-N_H\,\sigma(E)} \times \mathrm{apec}(kT, Z, z, norm),$$

where the exponential term represents photoelectric absorption by the interstellar medium, modeled with `phabs`. Here, $N_H$ is the equivalent hydrogen column density (in $\mathrm{cm}^{-2}$), and $\sigma(E)$ is the photoelectric cross-section. The `apec` component describes a collisionally-ionized, optically thin plasma, appropriate for ICM conditions (Section 1.3). It has the following parameters:

- $kT$ — electron temperature of the plasma (keV),
- $Z$ — metal abundance relative to solar,
- $z$ — redshift,

- norm — a factor proportional to the emission measure:

$$norm = \frac{10^{-14}}{4\pi[D_A(1+z)]^2} \int n_e n_H \, dV \tag{3.1}$$

  where $n_e$ and $n_H$ are the electron and hydrogen densities ($\mathrm{cm}^{-3}$), and $D_A$ is the angular diameter distance (cm).

The second model used was `phabs*vapec`, an extension of `apec` that allows individual elemental abundances to be varied separately. This model is particularly useful for investigating chemical enrichment history through detection of element-specific line emission. Elements such as Fe, Si, S, Mg, O, and Ni were individually fit where signal-to-noise permitted. The underlying physical assumptions are the same as in `apec`, but instead of a single metallicity value, the `vapec` model includes independent parameters for each detectable element.

### 3.4.2. Fitting Method

During spectral fitting, the redshift was fixed to $z = 0.0943$, and $N_H$ was fixed to the Galactic value of $2.56 \times 10^{20}$ $\mathrm{cm}^{-2}$ [95]. The elemental abundance table was set to the solar values from [96].

The energy range for fitting was set to 0.5–7.0 keV for *XMM-Newton* and 0.5–8.0 keV for *Chandra*, excluding known instrumental background features and calibration artifacts (e.g., 1.5–1.8 keV for MOS cameras due to Al-K lines).

Table 1.1 lists the major fluorescent instrumental lines present in the XMM-Newton MOS and PN detectors. These arise from interactions of high-energy particles with detector materials and must be considered or excluded during spectral modeling, depending on the energy range of interest.

Each spectrum was initially fit with the simpler `apec` model to determine the overall temperature and metallicity. Subsequently, the `vapec` model was applied to search for individual elemental abundances where the data quality allowed.

Goodness-of-fit was evaluated using the reduced chi-squared value, and errors were calculated at the 90% confidence level.

This two-step modeling strategy allowed us to obtain both a broad characterization of the thermal structure of the ICM and a more nuanced view of its chemical composition, providing valuable insight into the enrichment history and merger dynamics of the cluster.

### 3.4.3. Background Spectra

Accurate modeling of the X-ray background is critical for reliable spectral analysis, especially in extended sources like galaxy clusters. In this study, background spectra for both *XMM-Newton* and *Chandra* were extracted from nearby, source-free circular regions located on the same CCD chip as the cluster emission. These regions were carefully chosen to avoid contamination from point sources and to reflect the local instrumental and particle background.

For XMM-Newton, background regions were selected from nearby areas with no visible sources and minimal cluster emission. The background spectra were extracted using SAS tasks and later included in XSPEC during spectral fitting. We did not use blank-sky backgrounds or filter-wheel-closed data; instead, we relied on local background estimation to ensure spatial consistency and match the detector response.

For Chandra, a similar approach was followed. A background region was manually defined in SAOImage DS9 and saved as a separate region file. During spectral extraction using the `specextract` task, this region was used to generate the background spectrum alongside the source spectrum and response files. The background was assigned in XSPEC using the `backgrnd` command, allowing proper subtraction and propagation of statistical uncertainties.

All background regions were visually inspected in both soft and hard X-ray images to ensure they were free from residual cluster emission and unresolved point sources.

This local background strategy offers a practical and reliable solution for systems like A2384, where blank-sky or off-field background data may not fully represent the local environment.

### 3.4.4. Model Fitting

Each region was fitted independently using XSPEC (version 12.13.1). For *XMM-Newton*, spectra from the PN, MOS1, and MOS2 detectors were used simultaneously. Since the detectors have different responses and effective areas, a multiplicative `constant` component was included in all models to correct for inter-instrument calibration differences. The constant was fixed at 1.0 for the PN detector, while it was left free to vary for MOS1 and MOS2.

The spectral files (.pi), along with their corresponding response matrix files (RMFs) and ancillary response files (ARFs), were loaded into XSPEC as separate data groups. Instrumental background models were included per group where appropriate. Background spectra were either subtracted during extraction or included explicitly using the `backgrnd` keyword.

For *Chandra*, spectra were extracted using the `specextract` task in CIAO. Each spectrum was accompanied by automatically generated RMF and ARF files. Local background was extracted from source-free regions on the same ACIS-S chip and used directly in the fit. Chandra spectra were modeled separately from XMM data, following the same strategy. The fit included a `constant` component fixed at 1.0, as only a single detector (ACIS) was involved.

Because some spectra contained relatively low counts, particularly in fainter regions or outer annuli, we adopted the C-statistic for spectral fitting. Grouping was done at a minimum of 1 count per bin using `grppha`. For background-subtracted spectra (as in our case), XSPEC automatically uses the W-statistic, which is the modified version of C-stat suitable for such data.

Once acceptable fits were achieved, evaluated based on the stability of model parameters and visual inspection of residuals, we used the `error` command to calculate 90% confidence intervals for key physical parameters such as temperature, normalization, and metallicity. These uncertainties are reported in Table 4.17-4.20 as ± values.

The resulting spectral plots for each region are presented in the next chapter. For XMM-Newton fits, each plot includes the PN, MOS1, and MOS2 spectra and their associated models.For Chandra fits, the ACIS-S spectrum is shown along with the best-fit thermal model and background components where applicable.

# 4. RESULTS

In this analysis, we adopted the following fixed parameters during spectral modeling:

(i) Galactic hydrogen column density, $N_H = 2.56 \times 10^{20}$ cm$^{-2}$
(ii) Redshift, $z = 0.0943$

The redshift value of $z = 0.0943$ for A2384 was obtained from the NASA/IPAC Extragalactic Database (NED) [97]. The Galactic hydrogen column density $N_H = 2.56 \times 10^{20}$ cm$^{-2}$ was determined using the HI4PI survey data [95], accessed via the online "nH Column Density Calculator" provided by HEASARC [98], using the sky coordinates of A2384.

Figures and Tables 4.5–4.16 and 4.1–4.8 present the resulting spectra, best-fit parameters, and fit statistics for the *Chandra*/ACIS and *XMM-Newton*/EPIC observations of the A2384 subcluster regions, respectively.

## 4.1. XMM-Newton Results

The following are the results from XMM-Newton data.

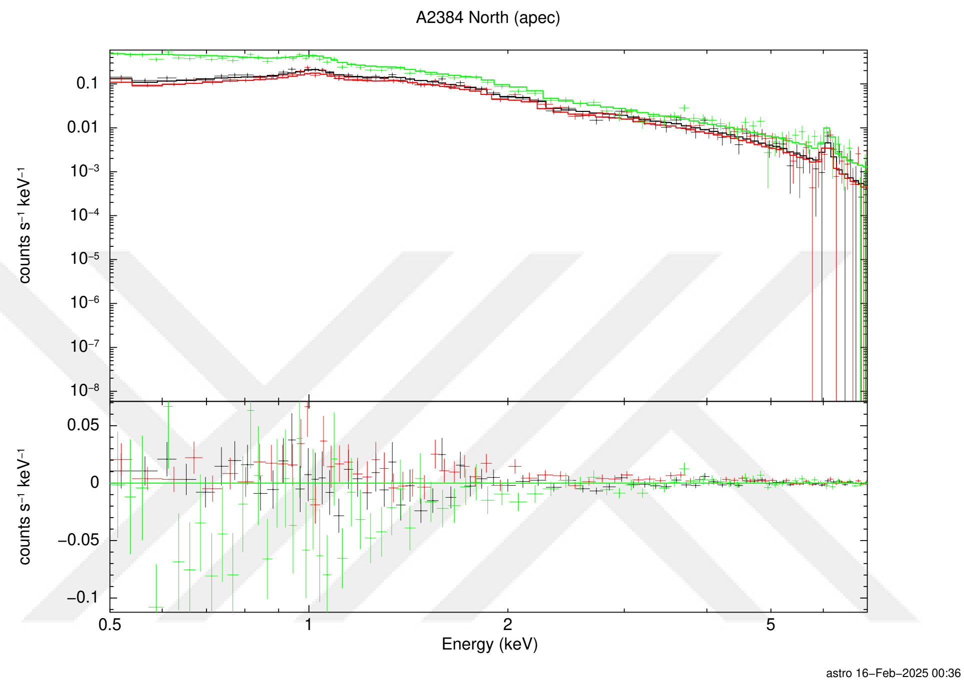


Figure 4.1. Fitting of A2384 North Region spectra using the APEC thermal plasma model

Table 4.1. Best-fit parameters of the VAPEC model for the A2384 North Region

| **VAPEC** | | | | | | |
|---|---|---|---|---|---|---|
| **kT**(keV) | **Ne** | **Mg** | **Si** | **S** | **Fe** | $\chi^2$ (d.o.f.) |
| $3.00^{+0.14}_{-0.14}$ | $0.63^{+0.54}_{-0.53}$ | $0.77^{+0.36}_{-0.17}$ | $0.31^{+0.40}_{-0.10}$ | $0.68^{+0.61}_{-0.59}$ | $0.30^{+0.10}_{-0.12}$ | 2228(2599) |

Table 4.2. Best-fit parameters of the APEC model for the A2384 North Region

| **APEC** | | |
|---|---|---|
| **kT** (keV) | **Abundance** ($Z_\odot$) | $\chi^2$ (d.o.f.) |
| $3.09^{+0.14}_{-0.13}$ | $0.29^{+0.06}_{-0.05}$ | 2228(2599) |

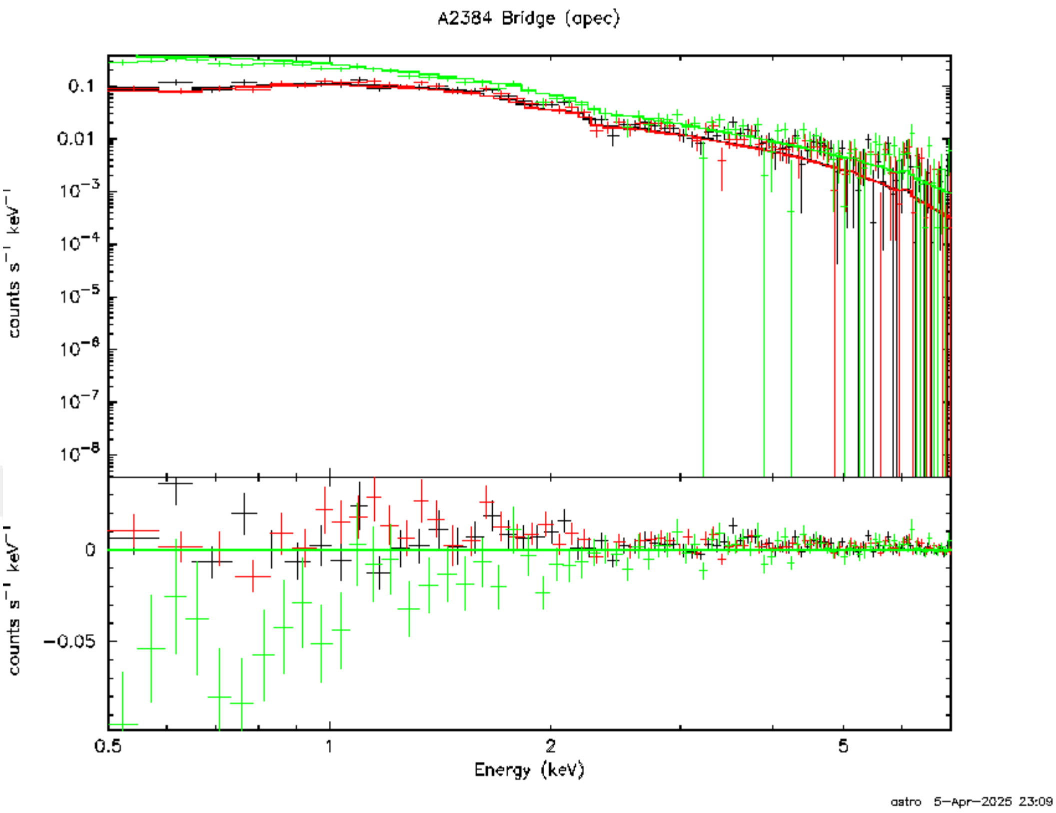


Figure 4.2. Fitting of Bridge 1 Region spectra using the APEC thermal plasma model

Table 4.3. Best-fit parameters of the VAPEC model for the Bridge 1 Region

| **VAPEC** | | | | | |
|---|---|---|---|---|---|
| **kT**(keV) | **Ne** | **Mg** | **Si** | **Fe** | $\chi^2$ (d.o.f.) |
| $3.03^{+0.20}_{-0.20}$ | $0.14^{+0.13}_{-0.14}$ | $0.78^{+0.76}_{-0.62}$ | $0.51^{+0.57}_{-0.51}$ | $0.15^{+0.15}_{-0.13}$ | 2091(2769) |

Table 4.4. Best-fit parameters of the APEC model for the Bridge 1 Region

| **APEC** | | |
|---|---|---|
| **kT** (keV) | **Abundance** ($Z_\odot$) | $\chi^2$ (d.o.f.) |
| $3.22^{+0.22}_{-0.22}$ | $0.11^{+0.08}_{-0.08}$ | 3073(3902) |

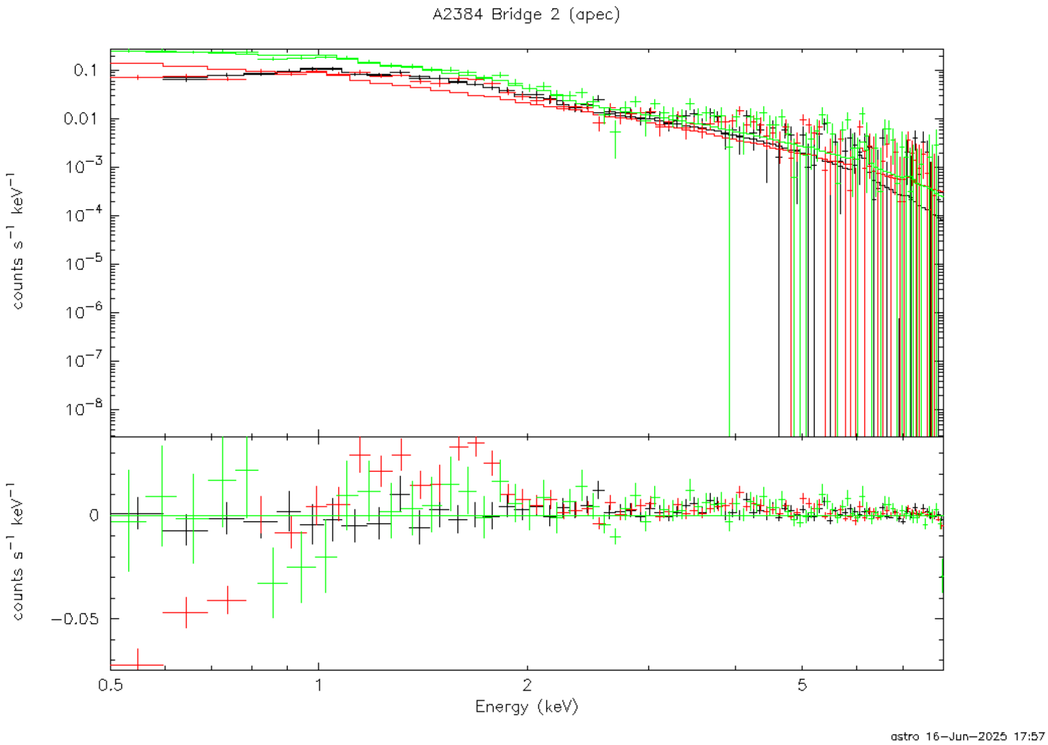


Figure 4.3. Fitting of Bridge 2 Region spectra using the APEC thermal plasma model

Table 4.5. Best-fit parameters of the APEC model for the Bridge 1 Region

| VAPEC | | | | |
|---|---|---|---|---|
| **kT**(keV) | **S** | **Mg** | **Fe** | $\chi^2$ (d.o.f.) |
| $2.53^{+0.18}_{-0.19}$ | $0.65^{+0.51}_{-0.46}$ | $0.34^{+0.50}_{-0.34}$ | $0.23^{+0.15}_{-0.13}$ | 2742 (2601) |

Table 4.6. Best-fit parameters of the APEC model for the Bridge 2 Region

| APEC | | |
|---|---|---|
| **kT** (keV) | **Abundance** ($Z_\odot$) | $\chi^2$ (d.o.f.) |
| $4.35^{+0.74}_{-0.60}$ | $0.22^{+0.12}_{-0.12}$ | 2742 (2601) |

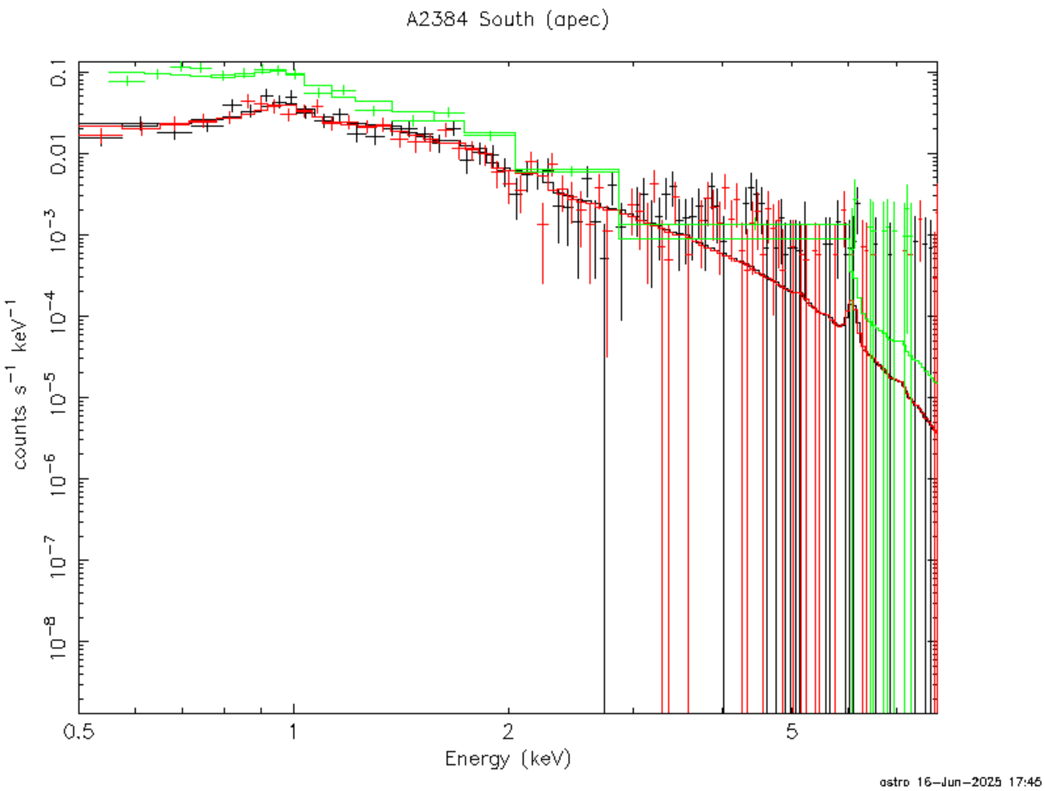


Figure 4.4. Fitting of A2384 South Region spectra using the APEC thermal plasma model

Table 4.7. Best-fit parameters of the VAPEC model for the A2384 South Region

| **VAPEC** | | | | |
|---|---|---|---|---|
| **kT**(keV) | **Si** | **S** | **Fe** | $\chi^2$ (d.o.f.) |
| $1.64^{+0.15}_{-0.17}$ | $0.20^{+0.31}_{-0.23}$ | $0.17^{+0.28}_{-0.17}$ | $0.10^{+0.04}_{-0.03}$ | 3612(3410) |

Table 4.8. Best-fit parameters of the APEC model for the A2384 South Region

| **APEC** | | |
|---|---|---|
| **kT** (keV) | **Abundance** ($Z_\odot$) | $\chi^2$ (d.o.f.) |
| $1.64^{+0.15}_{-0.17}$ | $0.18^{+0.02}_{-0.02}$ | 3612(3410) |

## 4.2. Chandra Results

The following are the results from Chandra data.

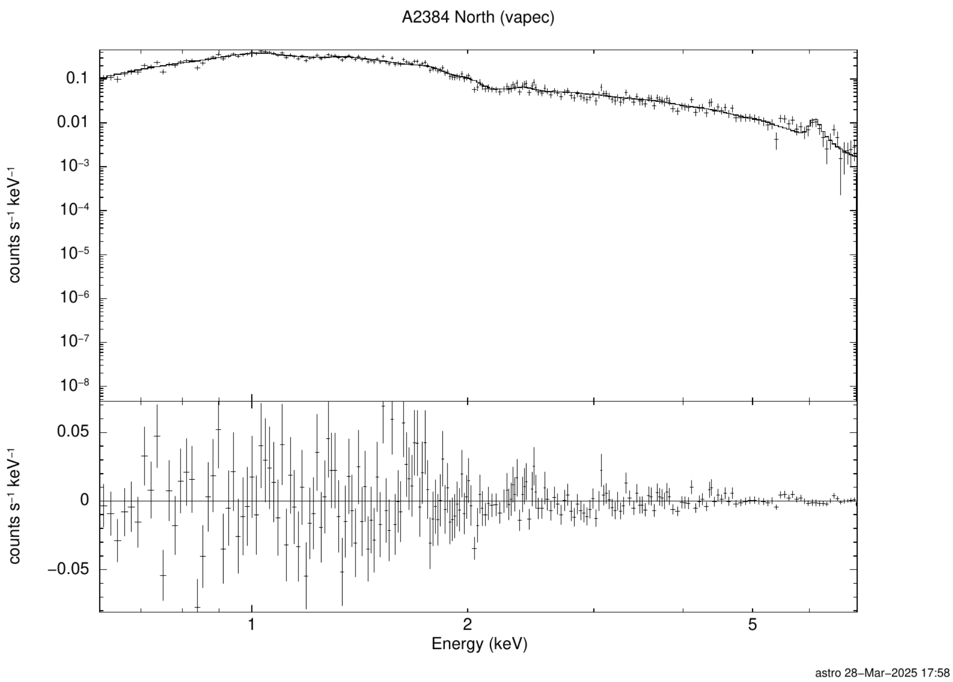


Figure 4.5. Fitting of A2384 North Region spectra using the VAPEC thermal plasma model

Table 4.9. Best-fit parameters of the VAPEC model for the A2384 North Region

| **VAPEC** | | | | | |
|---|---|---|---|---|---|
| **kT**(keV) | **Ne** | **Mg** | **S** | **Fe** | $\chi^2$ (d.o.f.) |
| $3.68^{+0.15}_{-0.14}$ | $0.76^{+0.76}_{-0.68}$ | $0.53^{+0.57}_{-0.51}$ | $0.40^{+0.41}_{-0.39}$ | $0.23^{+0.05}_{-0.06}$ | 547 (437) |

Table 4.10. Best-fit parameters of the APEC model for the A2384 North Region

| **APEC** | | |
|---|---|---|
| **kT** (keV) | **Abundance** ($Z_\odot$) | $\chi^2$ (d.o.f.) |
| $3.74^{+0.15}_{-0.14}$ | $0.31^{+0.07}_{-0.06}$ | 549 (368) |

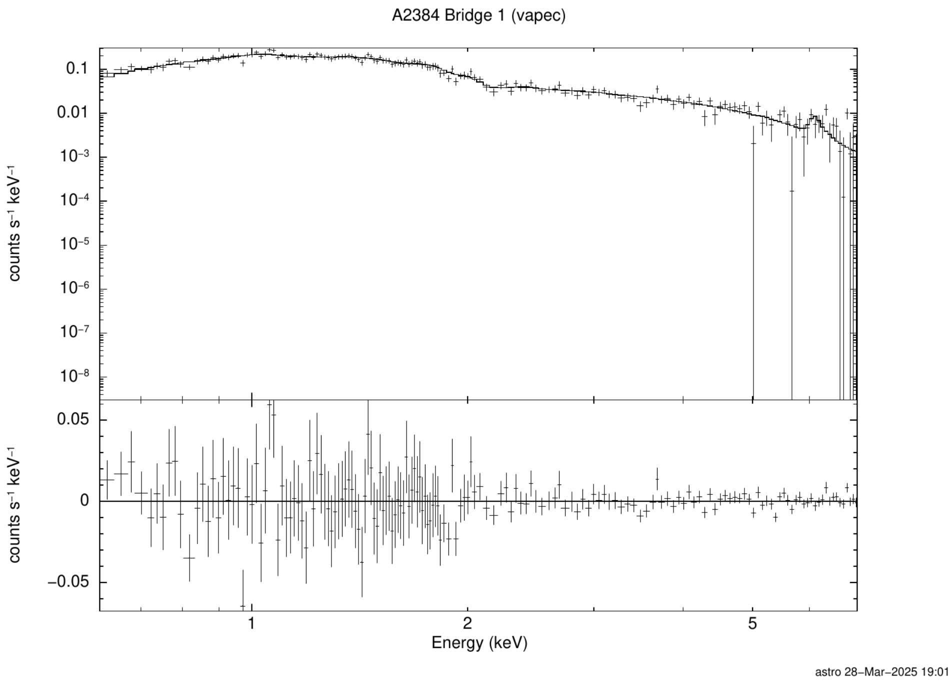


Figure 4.6. Fitting of Bridge 1 Region spectra using the VAPEC thermal plasma model

Table 4.11. Best-fit parameters of the VAPEC model for the Bridge 1 Region

| **VAPEC** | | | | | |
|---|---|---|---|---|---|
| **kT**(keV) | **Ne** | **Mg** | **S** | **Fe** | $\chi^2$ (d.o.f.) |
| $4.04^{+0.36}_{-0.28}$ | $0.16^{+1.36}_{-0.16}$ | $0.25^{+0.97}_{-0.24}$ | $0.16^{+0.80}_{-0.16}$ | $0.21^{+0.11}_{-0.09}$ | 428 (437) |

Table 4.12. Best-fit parameters of the APEC model for the Bridge 1 Region

| **APEC** | | |
|---|---|---|
| **kT** (keV) | **Abundance** ($Z_\odot$) | $\chi^2$ (d.o.f.) |
| $4.64^{+0.34}_{-0.34}$ | $0.27^{+0.13}_{-0.11}$ | 428 (437) |

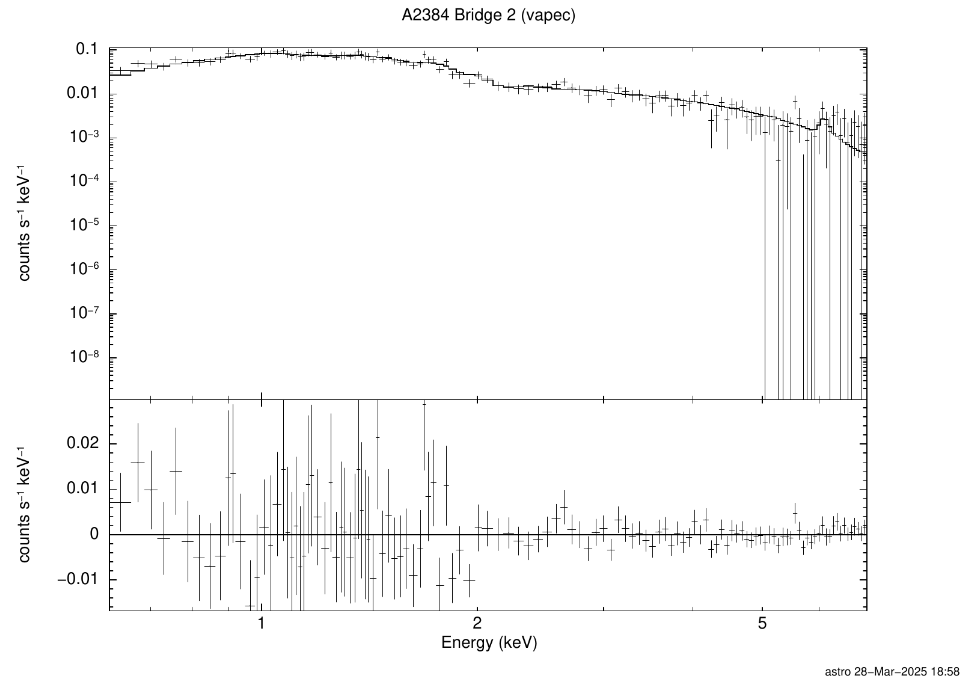


Figure 4.7. Best-fit parameters of the VAPEC model for the Bridge 2 Region

Table 4.13. Best-fit parameters of the VAPEC model for the A2384 Bridge 2 Region

| VAPEC | | | | |
|---|---|---|---|---|
| **kT**(keV) | **Ne** | **Mg** | **Fe** | $\chi^2(d.o.f.)$ |
| $4.39^{+0.58}_{-0.55}$ | $0.33^{+1.9}_{-0.33}$ | $0.38^{+1.3}_{-0.38}$ | $0.15^{+0.16}_{-0.12}$ | 430 (437) |

Table 4.14. Best-fit parameters of the APEC model for the Bridge 2 region.

| APEC | | |
|---|---|---|
| **kT** (keV) | **Abundance** ($Z_\odot$) | $\chi^2$ (d.o.f.) |
| $4.28^{+0.55}_{-0.51}$ | $0.19^{+0.18}_{-0.15}$ | 430 (437) |

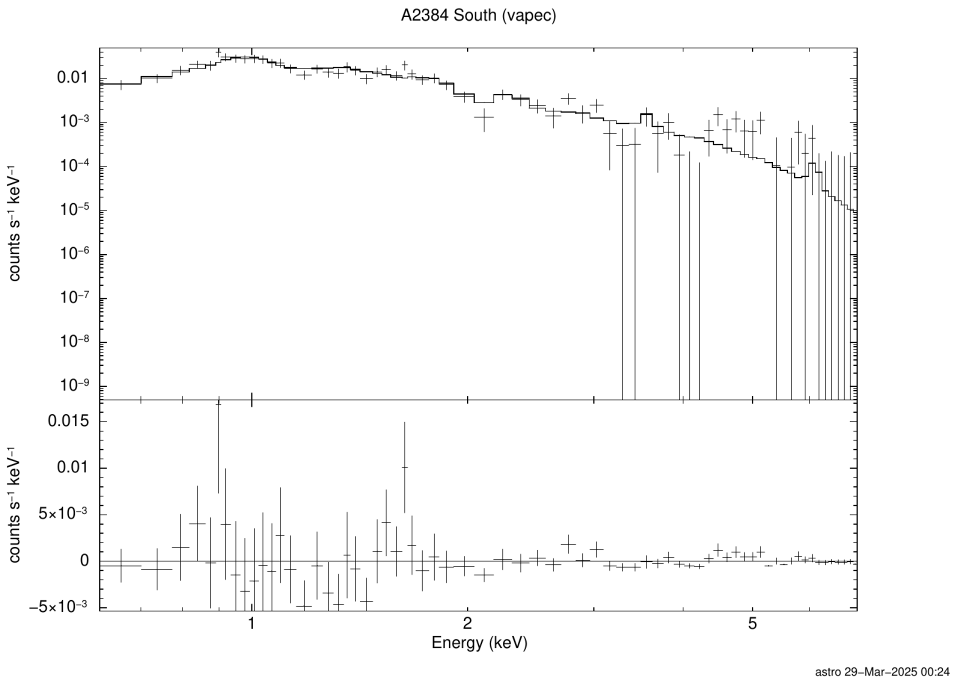


Figure 4.8. Best-fit parameters of the VAPEC model for the A2384 South Region

Table 4.15. Best-fit parameters of the VAPEC model for the A2384 South Region

| VAPEC | | | | |
|---|---|---|---|---|
| **kT**(keV) | **Si** | **S** | **Fe** | $\chi^2(d.o.f.)$ |
| $1.85^{+0.24}_{-0.20}$ | $0.26^{+0.33}_{-0.20}$ | $0.77^{+0.70}_{-0.52}$ | $0.20^{+0.25}_{-0.10}$ | 430 (437) |

Table 4.16. Best-fit parameters of the APEC model for the A2384 South Region

| APEC | | |
|---|---|---|
| **kT** (keV) | **Abundance** ($Z_\odot$) | $\chi^2(d.o.f.)$ |
| $1.67^{+0.27}_{-0.21}$ | $0.26^{+0.13}_{-0.11}$ | 1364(403) |

## 4.3. Thermal and Chemical Profiles of A2384

In order to investigate the thermodynamical and chemical structure of the intracluster medium (ICM) in the merging galaxy cluster A2384, we performed a spatially resolved X-ray spectral analysis based on data obtained from four distinct subregions. These regions, corresponding to the northern and southern subclusters as well as the two interconnecting bridge structures, were analyzed separately using observations from both *XMM-Newton* and *Chandra*.

The spectral fitting was carried out using the XSPEC software package, employing both the `apec` and `vapec` thermal plasma emission models. The `apec` model was used to derive the temperature ($kT$) and metallicity ($Z$) of the ICM in each region. In contrast, the `vapec` model allowed for individual elemental abundances—specifically those of neon (Ne), magnesium (Mg), silicon (Si), sulfur (S), and iron (Fe)—to be varied independently. This enabled a more refined chemical characterization of the ICM, particularly useful for tracing enrichment patterns linked to different types of supernovae (e.g., Type Ia vs. core-collapse).

For both telescopes and each region, the model parameters were constrained through $\chi^2$ minimization, and statistical uncertainties were computed using the `error` command in XSPEC, corresponding to the 90% confidence level for one interesting parameter. The resulting best-fit values are summarized in the following subsections. Detailed results obtained from the *XMM-Newton* data are presented in Section 4.3.1, while those derived from the *Chandra* observations are provided in Section 4.3.2. These measurements form the basis for our subsequent interpretation of the thermal state and chemical enrichment history of A2384's ICM.

### 4.3.1. XMM-Newton Results

Table 4.17 and Table 4.18 summarize the spectral fitting results for the four selected regions in the *XMM-Newton* data. The `apec` model provides estimates of the plasma temperature and overall metallicity, while the `vapec` model reveals individual elemental abundances.

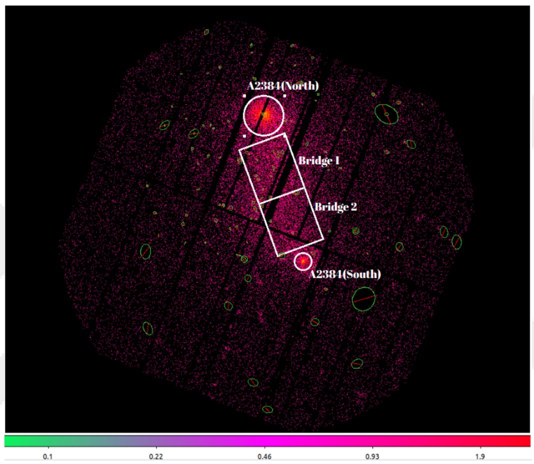


Figure 4.9. Selected regions shown on the PN camera image.

Table 4.17. Best-fit elemental abundances from the APEC model for XMM-Newton regions of A2384.

| **APEC** | | | | |
|---|---|---|---|---|
| **Region** | **A2384 (N)** | **Bridge 1** | **Bridge 2** | **A2384 (S)** |
| $kT$ **(keV)** | $3.09^{+0.14}_{-0.13}$ | $3.22^{+0.22}_{-0.22}$ | $4.35^{+0.74}_{-0.60}$ | $1.64^{+0.15}_{-0.17}$ |
| **Abundance** ($Z_{\odot}$) | $0.35^{+0.08}_{-0.07}$ | $0.11^{+0.08}_{-0.08}$ | $0.22^{+0.12}_{-0.12}$ | $0.18^{+0.02}_{-0.02}$ |
| $\chi^2$ **(d.o.f.)** | 2228 (2599) | 3037 (3902) | 2742 (2601) | 3612 (3410) |

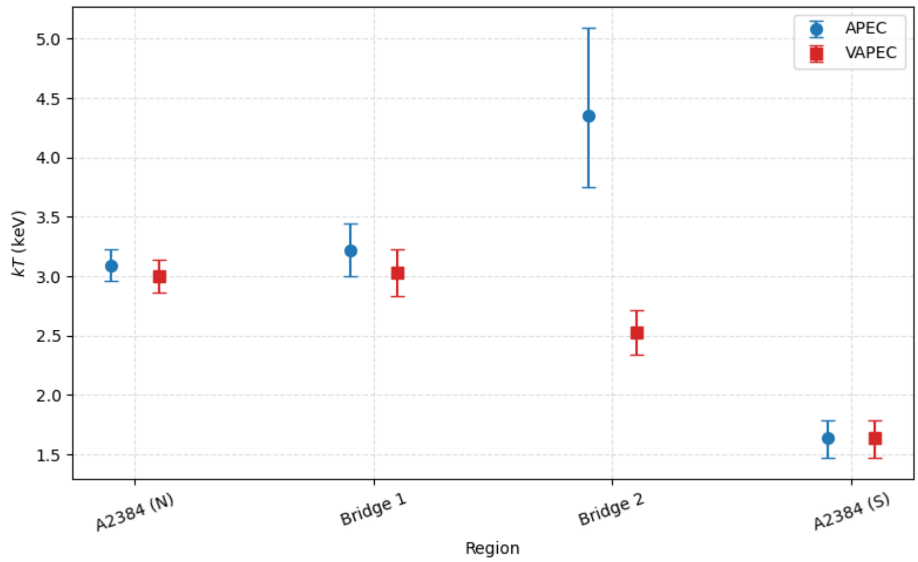


Figure 4.10. Temperature profile of A2384 subregions, derived from spectral fits with the APEC and VAPEC models based on *XMM-Newton* data.

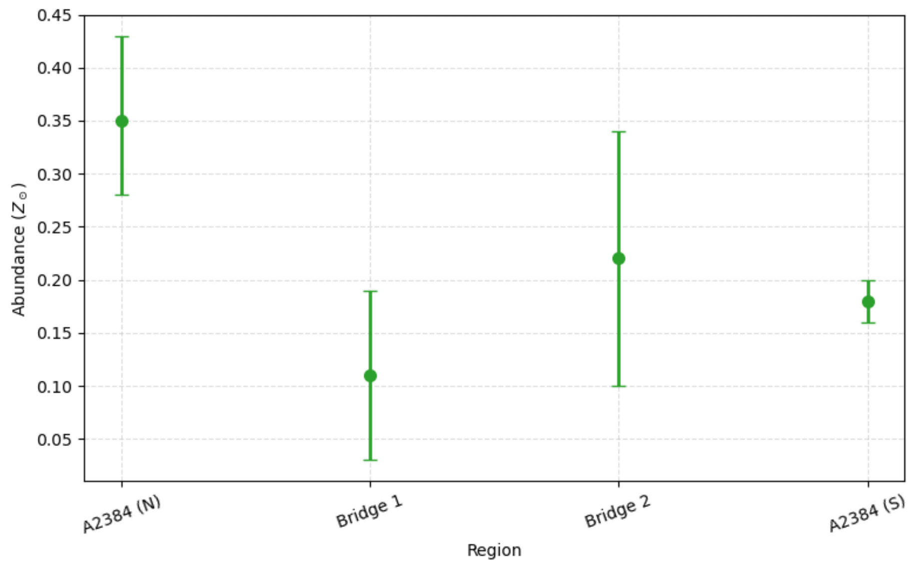


Figure 4.11. Elemental abundances across the A2384 subregions, derived from spectral fits with the APEC model using *XMM-Newton* data.

Table 4.18. Best-fit elemental abundances and plasma temperatures from the VAPEC model for Chandra regions of A2384.

| **VAPEC** | | | | |
|---|---|---|---|---|
| **Region** | **A2384 (N)** | **Bridge 1** | **Bridge 2** | **A2384 (S)** |
| $kT$ **(keV)** | $3.00^{+0.14}_{-0.14}$ | $3.03^{+0.20}_{-0.20}$ | $2.53^{+0.18}_{-0.19}$ | $1.64^{+0.15}_{-0.17}$ |
| **Ne** | $0.63^{+0.54}_{-0.53}$ | $0.14^{+0.13}_{-0.14}$ | $0.14^{+0.14}_{-0.13}$ | – |
| **Mg** | $0.77^{+0.36}_{-0.17}$ | $0.78^{+0.76}_{-0.62}$ | $0.34^{+0.50}_{-0.34}$ | – |
| **Si** | $0.31^{+0.40}_{-0.10}$ | $0.51^{+0.57}_{-0.51}$ | – | $0.20^{+0.31}_{-0.23}$ |
| **S** | $0.68^{+0.61}_{-0.59}$ | – | $0.65^{+0.51}_{-0.46}$ | $0.17^{+0.24}_{-0.24}$ |
| **Fe** | $0.30^{+0.10}_{-0.12}$ | $0.15^{+0.15}_{-0.13}$ | $0.23^{+0.15}_{-0.13}$ | $0.10^{+0.04}_{-0.03}$ |
| $\chi^2$ **(d.o.f.)** | 2228 (2599) | 2091 (2769) | 2742 (2601) | 3612 (3410) |

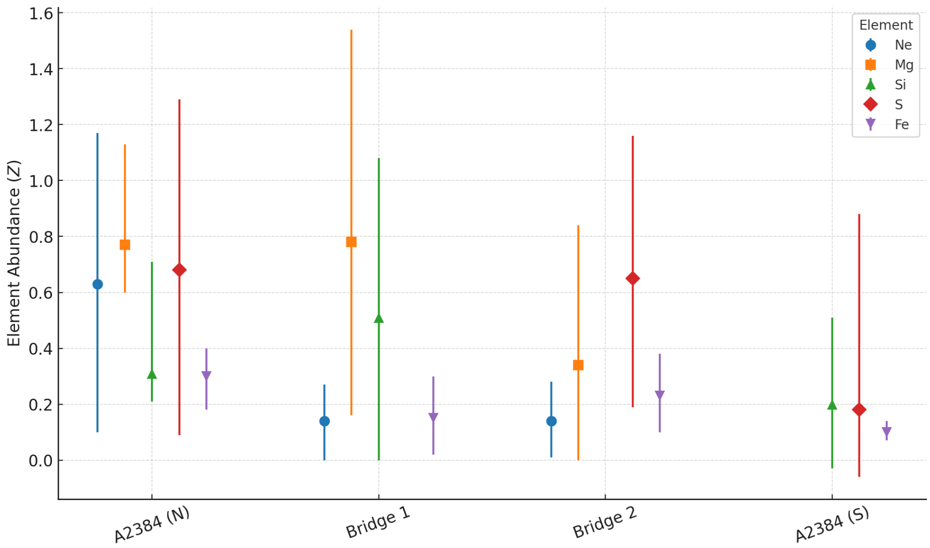


Figure 4.12. Comparison of elemental abundances (Fe, Mg, Ne, S, Si) derived from XMM-Newton spectra for four subregions of A2384: A2384 (N), A2384 (S), Bridge 1, and Bridge 2.

### 4.3.2. Chandra Results

Table 4.19 and Table 4.20 summarize the best-fit spectral parameters for the *Chandra* regions using `apec` and `vapec` models.

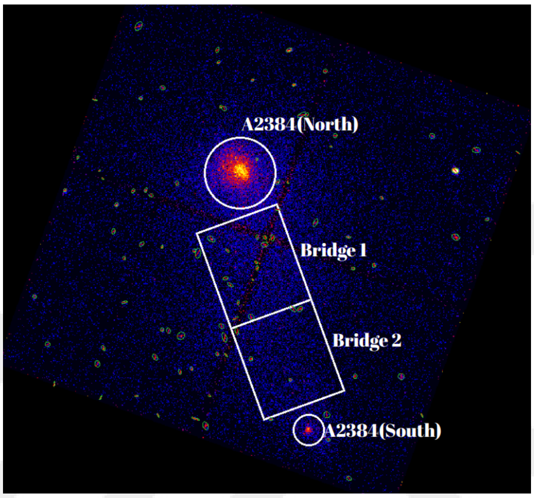


Figure 4.13. Selected regions shown on the PN camera image.

Table 4.19. Best-fit elemental abundances from the APEC model for Chandra regions of A2384.

| **APEC** | | | | |
|---|---|---|---|---|
| **Region** | **A2384 (N)** | **Bridge 1** | **Bridge 2** | **A2384 (S)** |
| $kT$ **(keV)** | $3.74^{+0.15}_{-0.14}$ | $4.64^{+0.34}_{-0.34}$ | $4.28^{+0.55}_{-0.51}$ | $1.67^{+0.27}_{-0.21}$ |
| **Abundance** ($Z_\odot$) | $0.31^{+0.07}_{-0.06}$ | $0.27^{+0.13}_{-0.11}$ | $0.19^{+0.18}_{-0.15}$ | $0.26^{+0.13}_{-0.11}$ |
| $\chi^2$ **(d.o.f.)** | 549 (368) | 428 (437) | 430 (437) | 1364 (403) |

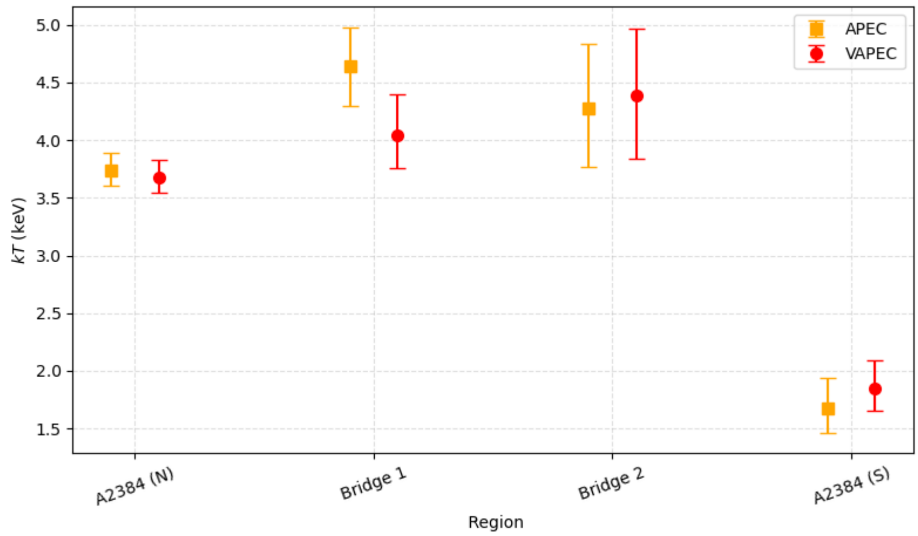


Figure 4.14. Temperature profile of A2384 subregions, derived from spectral fits with the APEC and VAPEC models using *Chandra* data.

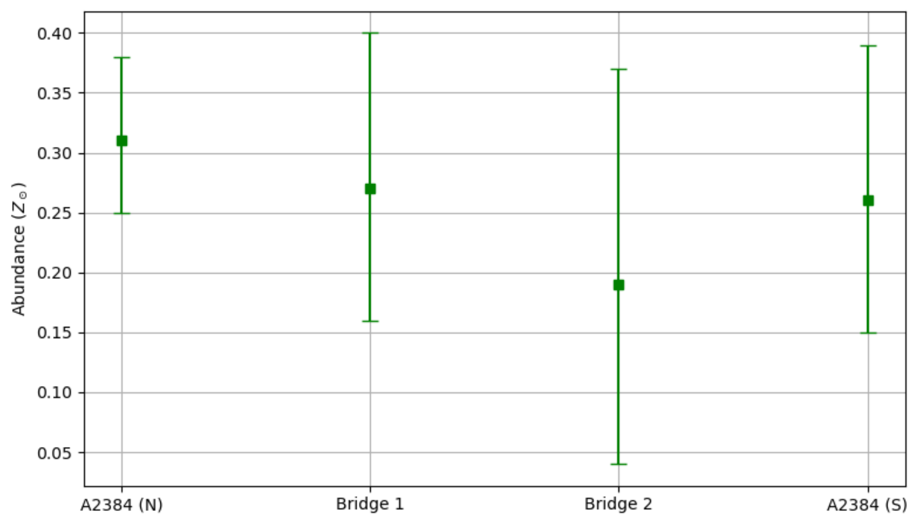


Figure 4.15. Elemental abundances across the A2384 subregions, derived from spectral fits with the APEC model using *Chandra* data.

Table 4.20. Best-fit elemental abundances and temperatures from the VAPEC model for Chandra regions of A2384.

| **VAPEC** | | | | |
|---|---|---|---|---|
| **Region** | **A2384 (N)** | **Bridge 1** | **Bridge 2** | **A2384 (S)** |
| $kT$ **(keV)** | $3.68^{+0.15}_{-0.14}$ | $4.04^{+0.36}_{-0.28}$ | $4.39^{+0.58}_{-0.55}$ | $1.85^{+0.24}_{-0.20}$ |
| **Ne** | $0.76^{+0.76}_{-0.68}$ | $0.16^{+1.36}_{-0.16}$ | $0.33^{+1.90}_{-0.33}$ | – |
| **Mg** | $0.53^{+0.57}_{-0.51}$ | $0.25^{+0.97}_{-0.24}$ | $0.38^{+1.30}_{-0.38}$ | – |
| **Si** | – | – | – | $0.26^{+0.33}_{-0.20}$ |
| **S** | $0.40^{+0.41}_{-0.39}$ | $0.16^{+0.80}_{-0.16}$ | $0.65^{+0.51}_{-0.46}$ | $0.77^{+0.70}_{-0.52}$ |
| **Fe** | $0.23^{+0.05}_{-0.06}$ | $0.21^{+0.11}_{-0.09}$ | $0.15^{+0.16}_{-0.12}$ | $0.20^{+0.25}_{-0.10}$ |
| $\chi^2$ **(d.o.f.)** | 547 (437) | 428 (437) | 430 (437) | 430 (403) |

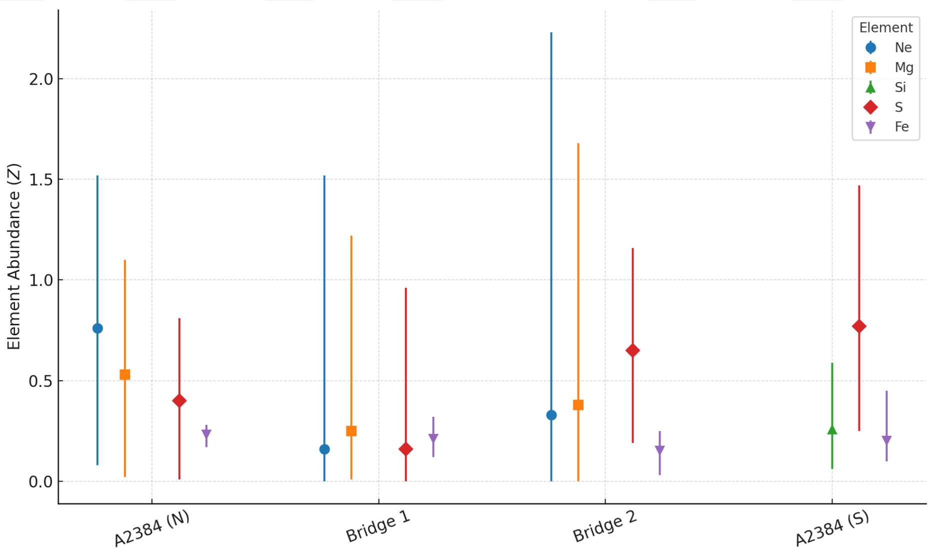


Figure 4.16. Comparison of elemental abundances (Fe, Mg, Ne, S, Si) derived from Chandra for four subregions of A2384: A2384 (N), A2384 (S), Bridge 1, and Bridge 2.

## 4.4. Discussion

Spatially resolved X-ray spectral analysis of the galaxy cluster A2384 using both *Chandra* and *XMM-Newton* data provides critical insights into its thermal structure and chemical enrichment history. By employing both the `apec` and `vapec` plasma models, we have explored not only global properties such as temperature and average metallicity, but also the individual elemental abundances across distinct regions within the cluster.

The APEC model results show that A2384 exhibits a mildly asymmetric thermal distribution. The northern region (A2384 North) has a lower temperature ($kT = 3.74^{+0.15}_{-0.14}$ keV), while the bridge and southern regions reach higher values ($kT \sim 4.3$–$4.6$ keV). This temperature structure aligns with the bimodal merger scenario proposed in previous studies [7, 90], where the southern component is likely still undergoing dynamical interactions, possibly affected by shock heating. The elevated temperatures in the bridge regions further support the presence of merger-driven heating, similar to what has been observed in clusters like A1758 [29].

The metallicity across all regions is relatively uniform, ranging from $Z \sim 0.19$ to $0.31, Z_\odot$, which is consistent with expectations for non-cool-core clusters. The lack of a central metallicity peak supports the hypothesis that A2384 is dynamically disturbed and has experienced metal redistribution due to merger-induced turbulence. Simulations suggest that such mergers can flatten metallicity gradients and disperse metals from the core throughout the ICM [6, 99].

The `vapec` model, which allows individual elemental abundances to vary, reveals a more detailed picture of A2384's chemical composition. In the northern region, elevated levels of Ne, Mg, and S are detected with relatively good constraints, while Fe remains modest ($\sim 0.24, Z_\odot$), pointing toward an enrichment history influenced by both Type Ia and core-collapse supernovae. The coexistence of $\alpha$-elements (like Mg and S) with Fe suggests a mixed contribution, which is also supported by theoretical nucleosynthesis models [58, 100].

Moreover, the best-fit temperatures derived from the `apec` and `vapec` models are in close agreement across all regions, indicating the robustness of the thermal structure derived from the X-ray spectral analysis. For the XMM-Newton data, these temperature values are presented in Figure 4.10 while the corresponding results from the Chandra data are summarized in Figure 4.14. The consistency between the two plasma models suggests that the thermal properties are not strongly affected by the choice of abundance modeling, reinforcing the reliability of the derived temperature distribution across the cluster.

In the bridge regions, where the signal-to-noise ratio is lower, the detection of individual elements is more uncertain, but Fe is consistently measured and remains below solar values. This could indicate that the enrichment in these transitional areas is dominated by more uniform metal mixing or possibly that contributions from Type Ia supernovae are less prominent.

The southern region shows relatively high S and Ca abundances (though with large uncertainties), which may reflect recent enrichment episodes or projection effects. Notably, high Ca abundance is uncommon and has been associated with complex supernova mixing scenarios in other clusters [101]. However, due to the large error bars, caution must be taken in interpreting these outliers.

The absence of strong Fe peaks and the roughly solar ratios between $\alpha$-elements and Fe are consistent with observations in other dynamically active, non-cool-core clusters such as Coma and Abell 3395 [3, 11].

Together, the thermal and chemical findings support the interpretation of A2384 as a post-merger system. The presence of high temperatures in the bridge, moderate and spatially uniform metallicities, and dispersed elemental abundances all point to a scenario in which the ICM has been heated and chemically mixed due to a major merger event.

The detection of $\alpha$-elements in different regions with varying levels may trace older episodes of enrichment by core-collapse supernovae, while the subsolar Fe and lack of metallicity gradients suggest that the mixing and redistribution mechanisms have had enough time to erase any localized enrichment from the brightest cluster galaxy (BCG).

These findings are in line with simulations and observations that demonstrate how mergers disrupt metallicity peaks, heat the gas, and produce complex spatial structures in both temperature and chemical content [9, 99, 102].

# 5. CONCLUSION

In this thesis, the Abell 2384 ($z \approx 0.0943$) galaxy cluster, which is in the post-merger phase, is studied by detailed spectral analysis and modeling, and these studies provide important findings in understanding the effects of post-merger dynamics on the intracluster medium (ICM). Through detailed analysis using phabs $*$ vapec and phabs$*$apec models, the subclusters A2384(N) and A2384(S), as well as the bridge connecting these clusters, were analyzed using XMM-Newton/EPIC and Chandra/ACIS observations. The temperature and metal abundance profiles were presented, and the temperature and metal abundance values obtained from different regions of the galaxy cluster were compared.

The results of the XMM-Newton analysis revealed that the temperature in the A2384(N) region is 2.87 keV, while in the bridge regions, it was measured as 3.32 keV and 4.35 keV, respectively. This temperature difference clearly indicates that shock waves formed in the post-merger bridge regions have heated the intracluster medium. As a result of the modeling, the metallicities of the selected regions were measured as 0.35 $Z_{\odot}$, 0.11 $Z_{\odot}$, 0.22 $Z_{\odot}$, and 0.18 $Z_{\odot}$, respectively.

According to Chandra analysis results, the temperature in the A2384(N) region is 3.74 keV, while it rises to 4.64 keV and 4.28 keV in Bridge 1 and Bridge 2 regions, respectively. In the A2384(S) region, the temperature was observed to decrease to 1.67 keV.

The metallicity values are 0.31 $Z_{\odot}$ for the A2384(N) region, 0.27 $Z_{\odot}$ for Bridge 1, and decrease to 0.19 $Z_{\odot}$ for Bridge 2, while in the A2384(S) region, it increases to 0.26 $Z_{\odot}$. This indicates that the A2384(N) and A2384(S) regions are richer in metal abundance compared to Bridge 1 and Bridge 2 regions.

The temperature difference observed as a result of the observations and analyses with the two satellites clearly demonstrates that shock waves formed in the post-merger bridge regions have heated the intracluster medium. Through modeling, the individual elemental abundances of the regions A2384(N), Bridge 1, Bridge 2, and A2384(S) were measured and are presented in Table 4.18 and Table 4.20.

The temperature (Figure4.10 and 4.14) and metal abundance profiles of the intracluster (Figure 4.11 and 4.15) gas determined for each region provide important insights into how the metal enrichment in galaxies has increased due to supernova explosions. The abundance ratios of iron and other heavy elements reflect the effects of chemical enrichment shaped by post-merger supernova contributions. Specifically, the increased metal abundance observed in the bridge regions indicates that gas flows and shock waves between galaxy clusters directly contribute to the chemical enrichment of the intracluster medium. These differing metal abundances observed in the bridge regions offer significant clues about how gas movements and shock effects in galaxy cluster mergers influence the chemical structure of the intracluster medium [6].

The modeling based on XMM-Newton observations shows that as we approach A2384(S) region is approached, the metal abundance increases; however, this increase begins to decrease in more distant subregions. This situation, as emphasized in the study by Parekh [90], points to the need for a more detailed examination of the radio source detected in this area. These findings provide significant insights into how the post-merger evolutionary process of the A2384 galaxy cluster affects the chemical and thermal structure of the intracluster gas.

# REFERENCES


1. Planck Collaboration, "Planck 2018 Results", *Astronomy and Astrophysics*, Vol. 641, p. A6, 2020.

2. Sarazin, C. L., "X-ray Emission from Clusters of Galaxies", *Reviews of Modern Physics*, Vol. 58, No. 1, pp. 1–115, 1986.

3. Mernier, F., V. Biffi, H. Yamaguchi, P. Medvedev, A. Simionescu, S. Ettori, N. Werner, J. S. Kaastra, J. De Plaa and L. Gu, "Enrichment of the Hot Intra-cluster Medium: Observations", *Space Science Reviews*, Vol. 214, No. 8, 2018.

4. Voit, G. M., "Tracing Cosmic Evolution with Clusters of Galaxies", *Reviews of Modern Physics*, Vol. 77, No. 1, pp. 207–258, 2005.

5. Fabian, A., "Observational Evidence of Active Galactic Nuclei Feedback", *Annual Review of Astronomy and Astrophysics*, Vol. 50, No. 1, pp. 455–489, 2012.

6. Mernier, F., J. De Plaa, C. Pinto, J. S. Kaastra, P. Kosec, Y.-y. Zhang, J. Mao and N. Werner, "Origin of Central Abundances in the Hot Intra-cluster Medium", *Astronomy and Astrophysics*, Vol. 592, p. A157, 2016.

7. Pranger, F., A. Böhm, C. Ferrari, S. Maurogordato, C. Benoist, H. Höller and S. Schindler, "Abell 2384: the Galaxy Population of a Cluster Post-merger", *Astronomy and Astrophysics*, Vol. 570, p. A40, 2014.

8. Parekh, V., K. Thorat, R. Kale, B. Hugo, N. Oozeer, S. Makhathini, D. Kleiner, S. V. White, G. I. G. Józsa, O. Smirnov, K. Van Der Heyden, S. Perkins, L. Andati, A. Ramaila and M. Ramatsoku, "MeerKAT's Discovery of a Radio Relic in the Bimodal Merging Cluster A2384", *Monthly Notices of the Royal Astronomical Society*, Vol. 499, No. 1, pp. 404–414, 2020.

9. McDonald, M., E. Bulbul, T. De Haan, E. D. Miller, B. A. Benson, L. E. Bleem, M. Brodwin, J. E. Carlstrom, I. Chiu, W. R. Forman, J. Hlavacek-Larrondo, G. P. Garmire, N. Gupta, J. J. Mohr, C. L. Reichardt, A. Saro, B. Stalder, A. A. Stark and J. D. Vieira, "The Evolution of the Intracluster Medium Metallicity in Sunyaev Zel'dovich-selected Galaxy Clusters at $0 < z < 1.5$ ", *The Astrophysical Journal*, Vol. 826, No. 2, p. 124, 2016.

10. Hlavacek-Larrondo, J., M. McDonald, B. A. Benson, W. R. Forman, S. W. Allen, L. E. Bleem, M. L. N. Ashby, S. Bocquet, M. Brodwin, J. P. Dietrich, C. Jones, J. Liu, C. L. Reichardt, B. R. Saliwanchik, A. Saro, T. Schrabback, J. Song, B. Stalder, A. Vikhlinin and A. Zenteno, "X-Ray Cavities in a Sample of 83 SPT-Selected Clusters of Galaxies: Tracing the Evolution of AGN Feedback in Clusters of Galaxies Out to $z = 1.2$", *The Astrophysical Journal*, Vol. 805, No. 1, p. 35, 2015.

11. Zhang, Y.-y., H. Andernach, C. A. Caretta, T. H. Reiprich, H. Böhringer, E. Puchwein, D. Sijacki and M. Girardi, "HIFLUGCS: Galaxy Cluster Scaling Relations Between X-ray Luminosity, Gas Mass, Cluster Radius, and Velocity Dispersion", *Astronomy and Astrophysics*, Vol. 526, p. A105, 2010.

12. Hoskin, M., *The Cambridge Concise History of Astronomy*, Cambridge University Press, Cambridge, 1999.

13. Wright, T., *An Original Theory or New Hypothesis of the Universe*, H. Chapelle, London, 1750.

14. Hubble, E., "Extragalactic Nebulae", *The Astrophysical Journal*, Vol. 64, pp. 321–369, 1926.

15. European Space Agency (ESA), 2025, "ESA Sky Online Tool", `https://sky.esa.int`, accessed: 15 May 2025.

16. Zwicky, F., "Die Rotverschiebung von Extragalaktischen Nebeln", *Helvetica Phys-*

*ica Acta*, Vol. 6, pp. 110–127, 1933.

17. Abell, G. O., "The Distribution of Rich Clusters of Galaxies", *The Astrophysical Journal Supplement Series*, Vol. 3, pp. 211–288, 1958.

18. Abell, G. O., H. G. Corwin and R. P. Olowin, "A Catalog of Rich Clusters of Galaxies. Part II - Northern and Southern Hemisphere Supplementary Catalog", *The Astrophysical Journal Supplement Series*, Vol. 70, pp. 1–138, 1989.

19. Gursky, H., A. Solinger, E. M. Kellogg, S. Murray, H. Tananbaum, R. Giacconi and A. Cavaliere, "X-Ray Emission from Rich Clusters of Galaxies", *The Astrophysical Journal*, Vol. 173, p. L99, 1972.

20. Jones, C. and W. Forman, "The Structure of Clusters of Galaxies Observed with Einstein.", *Astrophysical Journal*, Vol. 276, pp. 38–55, 1984.

21. Bohringer, H., W. Voges, J. P. Huchra, B. McLean, R. Giacconi, P. Rosati, R. Burg, J. Mader, P. Schuecker, D. Simic, S. Komossa, T. H. Reiprich, J. Retzlaff and J. Trumper, "The Northern ROSAT All-Sky (NORAS) Galaxy Cluster Survey. i. X-Ray Properties of Clusters Detected as Extended X-Ray Sources", *The Astrophysical Journal Supplement Series*, Vol. 129, No. 2, pp. 435–474, 2000.

22. Markevitch, M., T. J. Ponman, P. E. J. Nulsen, M. W. Bautz, D. J. Burke, L. P. David, D. Davis, R. H. Donnelly, W. R. Forman, C. Jones, J. Kaastra, E. Kellogg, D.-W. Kim, J. Kolodziejczak, P. Mazzotta, A. Pagliaro, S. Patel, L. Van Speybroeck, A. Vikhlinin, J. Vrtilek, M. Wise and P. Zhao, "Chandra Observation of A2142: Survival of Dense Subcluster Cores in a Merger", *The Astrophysical Journal*, Vol. 541, pp. 542–549, 2000.

23. Arnaud, M., N. Aghanim, R. Gastaud, D. M. Neumann, D. Lumb, U. Briel, B. Altieri, S. Ghizzardi, J. Mittaz, T. P. Sasseen and W. T. Vestrand, "XMM-Newton Observation of the Coma Galaxy Cluster - The Temperature Structure in the Central Region", *Astronomy & Astrophysics*, Vol. 365, pp. L67–L73, 2001.

24. Planck Collaboration, "Planck2015 results: XXVII. The Second Planck Catalogue of Sunyaev-Zeldovich Sources", *Astronomy & Astrophysics*, Vol. 594, p. A27, 2016.

25. Predehl, P., R. Andritschke, V. Arefiev, V. Babyshkin, O. Batanov, W. Becker, H. Böhringer, A. Bogomolov, T. Boller, K. Borm, W. Bornemann, H. Bräuninger, M. Brüggen, H. Brunner, M. Brusa, E. Bulbul, M. Buntov, V. Burwitz, W. Burkert, N. Clerc, E. Churazov, D. Coutinho, T. Dauser, K. Dennerl, V. Doroshenko, J. Eder, V. Emberger, T. Eraerds, A. Finoguenov, M. Freyberg, P. Friedrich, S. Friedrich, M. Fürmetz, A. Georgakakis, M. Gilfanov, S. Granato, C. Grossberger, A. Gueguen, P. Gureev, F. Haberl, O. Hälker, G. Hartner, G. Hasinger, H. Huber, L. Ji, A. v. Kienlin, W. Kink, F. Korotkov, I. Kreykenbohm, G. Lamer, I. Lomakin, I. Lapshov, T. Liu, C. Maitra, N. Meidinger, B. Menz, A. Merloni, T. Mernik, B. Mican, J. Mohr, S. Müller, K. Nandra, V. Nazarov, F. Pacaud, M. Pavlinsky, E. Perinati, E. Pfeffermann, D. Pietschner, M. E. Ramos-Ceja, A. Rau, J. Reiffers, T. H. Reiprich, J. Robrade, M. Salvato, J. Sanders, A. Santangelo, M. Sasaki, H. Scheuerle, C. Schmid, J. Schmitt, A. Schwope, A. Shirshakov, M. Steinmetz, I. Stewart, L. Strüder, R. Sunyaev, C. Tenzer, L. Tiedemann, J. Trümper, V. Voron, P. Weber, J. Wilms and V. Yaroshenko, "The eROSITA X-ray Telescope on SRG", *Astronomy & Astrophysics*, Vol. 647, p. A1, 2021.

26. Barret, D., T. Lam Trong, J.-W. den Herder, L. Piro, X. Barcons, J. Huovelin, R. Kelley, J. M. Mas-Hesse, K. Mitsuda, S. Paltani, G. Rauw, A. Rożanska, J. Wilms, M. Barbera, E. Bozzo, M. T. Ceballos, I. Charles, A. Decourchelle, R. den Hartog, J.-M. Duval, F. Fiore, F. Gatti, A. Goldwurm, B. Jackson, P. Jonker, C. Kilbourne, C. Macculi, M. Mendez, S. Molendi, P. Orleanski, F. Pajot, E. Pointecouteau, F. Porter, G. W. Pratt, D. Prêle, L. Ravera, E. Renotte, J. Schaye, K. Shinozaki, L. Valenziano, J. Vink, N. Webb, N. Yamasaki, F. Delcelier-Douchin, M. Le Du, J.-M. Mesnager, A. Pradines, G. Branduardi-Raymont, M. Dadina, A. Finoguenov, Y. Fukazawa, A. Janiuk, J. Miller, Y. Nazé, F. Nicastro, S. Sciortino, J. M. Torrejon, H. Geoffray, I. Hernandez, L. Luno, P. Peille, J. André, C. Daniel, C. Etcheverry, E. Gloaguen, J. Hassin, G. Hervet,

I. Maussang, J. Moueza, A. Paillet, B. Vella, G. Campos Garrido, J.-C. Damery, C. Panem, J. Panh, S. Bandler, J.-M. Biffi, K. Boyce, A. Clénet, M. DiPirro, P. Jamotton, S. Lotti, D. Schwander, S. Smith, B.-J. van Leeuwen, H. van Weers, T. Brand, B. Cobo, T. Dauser, J. de Plaa and E. Cucchetti, "The Athena X-ray Integral Field Unit (X-IFU)", *Astronomy & Astrophysics*, Vol. 636, p. A10, 2020.

27. Simionescu, A., N. Werner, H. Böhringer, J. S. Kaastra, A. Finoguenov, M. Brüggen and P. E. J. Nulsen, "Chemical Enrichment in the Cluster of Galaxies Hydra A", *Astronomy and Astrophysics*, Vol. 493, No. 2, pp. 409–424, 2008.

28. Mitchell, R. J., J. L. Culhane, P. J. N. Davison and J. C. Ives, "Ariel 5 Observations of the X-ray Spectrum of the Perseus Cluster", *Monthly Notices of the Royal Astronomical Society*, Vol. 175, No. 1, pp. 29P–34P, 1976.

29. Markevitch, M. and A. Vikhlinin, "Shocks and Cold Fronts in Galaxy Clusters", *Physics Reports*, Vol. 443, No. 1, pp. 1–53, 2007.

30. Ferrari, C., C. Benoist, S. Maurogordato, A. Cappi and E. Slezak, "Dynamical State and Star Formation Properties of the Merging Galaxy Cluster Abell 3921", *Astronomy and Astrophysics*, Vol. 430, No. 1, pp. 19–38, 2005.

31. Mazzotta, P., M. Markevitch, A. Vikhlinin, W. R. Forman, L. P. David and L. VanSpeybroeck, "Chandra Observation of RX J1720.1+2638: a Nearly Relaxed Cluster with a Fast-moving Core?", *The Astrophysical Journal*, Vol. 555, No. 1, pp. 205–214, 2001.

32. Sarazin, C. L., *The Physics of Cluster Mergers*, p. 1–38, Springer Netherlands, 2002.

33. Feretti, L., G. Giovannini, F. Govoni and M. Murgia, "Clusters of Galaxies: Observational Pproperties of the Diffuse Radio Emission", *The Astronomy and Astrophysics Review*, Vol. 20, No. 1, May 2012.

34. Brunetti, G., S. Giacintucci, R. Cassano, W. Lane, D. Dallacasa, T. Venturi, N. E. Kassim, G. Setti, W. D. Cotton and M. Markevitch, "A Low-frequency Radio Halo Associated with a Cluster of Galaxies", *Nature*, Vol. 455, pp. 944–947, 2008.

35. Brunetti, G. and T. W. Jones, "Cosmic Rays in Galaxy Clusters and Their Non-thermal Emission", *International Journal of Modern Physics D*, Vol. 23, No. 4, p. 1430007, 2014.

36. Monna, A., S. Seitz, A. Zitrin, M. J. Geller, C. Grillo, A. Mercurio, N. Greisel, A. Halkola, S. H. Suyu, M. Postman, P. Rosati, I. Balestra, A. Biviano, D. Coe, D. G. Fabricant, H. S. Hwang and A. Koekemoer, "Constraining the Galaxy Mass Content in the Core of A383 Using Velocity Dispersion Measurements for Individual Cluster Members", *Monthly Notices of the Royal Astronomical Society*, Vol. 447, No. 2, p. 1224–1241, 2014.

37. Breuer, J., N. Werner, F. Mernier, K. Umetsu, A. Simionescu, M. Devlin, L. Di Mascolo, T. Dibblee-Barkman, S. Dicker, B. Mason, T. Mroczkowski, C. Romero, C. Sarazin and J. Sievers, "The Thermodynamic Structure and Large-scale Structure Filament in MACS J0717.5+3745", *arXiv (Cornell University)*, 2024.

38. Pranger, F., A. Böhm, C. Ferrari, S. Maurogordato, C. Benoist, H. Höller and S. Schindler, "Abell 2384: the Galaxy Population of a Cluster Post-merger", *Astronomy & Astrophysics*, Vol. 570, p. A40, 2014.

39. XMM-Newton Science Operations Centre, 2025, "XMM-Newton Science Archive (XSA)", `https://www.cosmos.esa.int/web/xmm-newton/xsa`, accessed: 15 April 2025.

40. Kravtsov, A. V. and S. Borgani, "Formation of Galaxy Clusters", *Annual Review of Astronomy and Astrophysics*, Vol. 50, pp. 353–409, 2012.

41. Cassano, R., S. Ettori, S. Giacintucci, G. Brunetti, M. Markevitch, T. Venturi and

M. Gitti, "On the Connection Between Giant Radio Haloes and Cluster Mergers", *The Astrophysical Journal Letters*, Vol. 721, No. 1, pp. L82–L86, 2010.

42. Hallman, E. J., B. Alden, D. Rapetti, A. Datta and J. O. Burns, "Probing the Curious Case of a Galaxy Cluster Merger in Abell 115 with High-fidelity Chandra X-Ray Temperature and Radio Maps", *The Astrophysical Journal*, Vol. 859, No. 1, p. 44, May 2018.

43. Owers, M. S., P. E. J. Nulsen, W. J. Couch and M. Markevitch, "A Sample of Merging Clusters with Cold Fronts from the Chandra Archive", *The Astrophysical Journal*, Vol. 704, No. 2, p. 1349–1370, 2009.

44. van Weeren, R. J., F. de Gasperin, H. Akamatsu, M. Brüggen, L. Feretti, H. Kang, A. Stroe and F. Zandanel, "Diffuse Radio Emission from Galaxy Clusters", *Space Science Reviews*, Vol. 215, No. 1, 2019.

45. Sarazin, C. L., "X-ray Emission from Clusters of Galaxies", *Reviews of Modern Physics*, Vol. 58, No. 1, pp. 1–115, 1986.

46. Blandford, R., D. Meier and A. Readhead, "Relativistic Jets from Active Galactic Nuclei", *Annual Review of Astronomy and Astrophysics*, Vol. 57, pp. 467–509, 2019.

47. Peterson, J. R. and A. C. Fabian, "X-ray Spectroscopy of Cooling Clusters", *Physics Reports*, Vol. 427, No. 1, pp. 1–39, 2006.

48. Fabian, A. C., "Cooling Flows in Clusters of Galaxies", *Annual Review of Astronomy and Astrophysics*, Vol. 40, pp. 539–577, 2002.

49. Bethe, H. A., "Energy Production in Stars", *Physical Review*, Vol. 55, pp. 434–456, 1939.

50. Burbidge, E. M., G. R. Burbidge, W. A. Fowler and F. Hoyle, "Synthesis of the

Elements in Stars", *Reviews of Modern Physics*, Vol. 29, pp. 547–650, 1957.

51. Arcones, A. and F.-K. Thielemann, "Origin of the Elements", *The Astronomy and Astrophysics Review*, Vol. 31, No. 1, 2022.

52. Woosley, S. E., A. Heger and T. A. Weaver, "The Evolution and Explosion of Massive Stars", *Reviews of Modern Physics*, Vol. 74, No. 4, pp. 1015–1071, 2002.

53. Woosley, S. and T. Janka, "The Physics of Core-collapse Supernovae", *Nature Physics*, Vol. 1, No. 3, pp. 147–154, 2005.

54. Bethe, H. A., "Supernova Mechanisms", *Reviews of Modern Physics*, Vol. 62, No. 4, pp. 801–866, 1990.

55. Burrows, A., "Colloquium: Perspectives on Core-collapse Supernova Theory", *Reviews of Modern Physics*, Vol. 85, No. 1, pp. 245–261, 2013.

56. Janka, H.-T., "Explosion mechanisms of Core-Collapse Supernovae", *Annual Review of Nuclear and Particle Science*, Vol. 62, No. 1, pp. 407–451, 2012.

57. Thielemann, F. K., A. Arcones, R. Käppeli, M. Liebendörfer, T. Rauscher, C. Winteler, C. Fröhlich, I. Dillmann, T. Fischer, G. Martinez-Pinedo, K. Langanke, K. Farouqi, K. L. Kratz, I. Panov and I. K. Korneev, "What are the Astrophysical Sites for the r-process and the Production of Heavy Elements?", *Progress in Particle and Nuclear Physics*, Vol. 66, No. 2, pp. 346–353, 2011.

58. Nomoto, K., N. Tominaga, H. Umeda, C. Kobayashi and K. Maeda, "Nucleosynthesis Yields of Core-collapse Supernovae and Hypernovae, and Galactic Chemical Evolution", *Nuclear Physics A*, Vol. 777, pp. 424–458, 2006.

59. Matteucci, F. and S. Recchi, "On the Typical Timescale for the Chemical Enrichment from Type Ia Supernovae in Galaxies", *The Astrophysical Journal*, Vol. 558, No. 1, pp. 351–358, 2001.

60. Smartt, S. J., “Progenitors of Core-Collapse Supernovae”, *Annual Review of Astronomy and Astrophysics*, Vol. 47, No. 1, pp. 63–106, 2009.

61. Hillebrandt, W. and J. C. Niemeyer, “Type IA Supernova Explosion Models”, *Annual Review of Astronomy and Astrophysics*, Vol. 38, No. 1, pp. 191–230, 2000.

62. Nomoto, K., “Evolution of 8-10 Solar Mass Stars Toward Electron Capture Supernovae. I - Formation of Electron-degenerate O + NE + MG Cores”, *The Astrophysical Journal*, Vol. 277, p. 791, 1984.

63. Khokhlov, A. M., “Delayed Detonation Model for Type IA Supernovae”, *Astronomy & Astrophysics*, Vol. 245, No. 1, pp. 114–128, 1991.

64. Riess, A. G., A. V. Filippenko, P. Challis, A. Clocchiatti, A. Diercks, P. M. Garnavich, R. L. Gilliland, C. J. Hogan, S. Jha, R. P. Kirshner, B. Leibundgut, M. M. Phillips, D. Reiss, B. P. Schmidt, R. A. Schommer, R. C. Smith, J. Spyromilio, C. Stubbs, N. B. Suntzeff and J. Tonry, “Observational Evidence from Supernovae for an Accelerating Universe and a Cosmological Constant”, *The Astronomical Journal*, Vol. 116, No. 3, pp. 1009–1038, 1998.

65. Perlmutter, S., G. Aldering, G. Goldhaber, R. A. Knop, P. Nugent, P. G. Castro, S. Deustua, S. Fabbro, A. Goobar, D. E. Groom, I. M. Hook, A. G. Kim, M. Y. Kim, J. C. Lee, N. J. Nunes, R. Pain, C. R. Pennypacker, R. Quimby, C. Lidman, R. S. Ellis, M. Irwin, R. G. McMahon, P. Ruiz-Lapuente, N. Walton, B. Schaefer, B. J. Boyle, A. V. Filippenko, T. Matheson, A. S. Fruchter, N. Panagia, H. J. M. Newberg, W. J. Couch and S. C. Project, “Measurements of $\Omega$ and $\Lambda$ from 42 High-Redshift Supernovae”, *The Astrophysical Journal*, Vol. 517, No. 2, pp. 565–586, 1999.

66. Seitenzahl, I. R., F. Ciaraldi-Schoolmann, F. K. Röpke, M. Fink, W. Hillebrandt, M. Kromer, R. Pakmor, A. J. Ruiter, S. A. Sim and S. Taubenberger, “Three-dimensional Delayed-detonation Models with Nucleosynthesis for Type Ia Supernovae”, *Monthly Notices of the Royal Astronomical Society*, Vol. 429, No. 2, pp.

1156–1172, 2012.

67. Kasen, D., B. Metzger, J. Barnes, E. Quataert and E. Ramirez-Ruiz, "Origin of the Heavy Elements in Binary Neutron-star Mergers from a Gravitational-wave Event", *Nature*, Vol. 551, No. 7678, pp. 80–84, 2017.

68. Durret, F., J. S. Kaastra, J. Nevalainen, T. Ohashi and N. Werner, "Soft X-Ray and Extreme Ultraviolet Excess Emission from Clusters of Galaxies", *Space Science Reviews*, Vol. 134, No. 1-4, pp. 51–70, 2008.

69. Böhringer, H. and N. Werner, "X-ray Spectroscopy of Galaxy Clusters: Studying Astrophysical Processes in the Largest Celestial Laboratories", *The Astronomy and Astrophysics Review*, Vol. 18, No. 1-2, p. 127–196, 2010.

70. Karzas, W. J. and R. Latter, "Electron Radiative Transitions in a Coulomb Field", *The Astrophysical Journal Supplement Series*, Vol. 6, No. 1, pp. 167–212, 1961.

71. de Plaa, J., "The Origin of the Chemical Elements in Cluster Cores", *Astronomische Nachrichten*, Vol. 334, No. 4, pp. 416–419, 2013.

72. Snowden, S. L. and Kuntz, K. D., 2016, "XMM-Newton ABC Guide to Background Analysis, Version 5.6", `http://labx.iasfbo.inaf.it/2018/resources/xmm_abc_guide.pdf`, accessed: 16 April 2025.

73. Iakubovskyi, D., "New Emission Line at 3.5 keV - Observational Status, Connection with Radiatively Decaying Dark Matter and Directions for Future Studies", *Advances in Astronomy and Space Physics*, Vol. 4, No. 1-2, pp. 9–14, 2014.

74. Foster, A. R., L. Ji, R. K. Smith and N. S. Brickhouse, "Updated Atomic DATA and Calculations for X-ray Spectroscopy", *The Astrophysical Journal*, Vol. 756, No. 2, p. 128, 2012.

75. Arnaud, K. A. and Gordon, C. A. and Dorman, B. and Rutkowski, K., 2025,

"An X-Ray Spectral Fitting Package: User's Guide for Version 12.15.0", https://heasarc.gsfc.nasa.gov/xanadu/xspec/manual/manual.html, accessed: 15 March 2025.

76. Jansen, F., D. Lumb, B. Altieri, J. Clavel, M. Ehle, C. Erd, C. Gabriel, M. Guainazzi, P. Gondoin, R. Much, R. Munoz, M. Santos, N. Schartel, D. Texier and G. Vacanti, "XMM-Newton Observatory. I. The Spacecraft and Operations", *Astronomy and Astrophysics*, Vol. 365, pp. L1–L6, 2001.

77. Lumb, D. H., N. Schartel and F. A. Jansen, "X-ray Multi-mirror Mission (XMM-Newton) observatory", *Optical Engineering*, Vol. 51, No. 1, 2012.

78. National Aeronautics and Space Administration (NASA), 2025, "XMM-Newton: A Space Observatory Studying the X-ray Universe", https://science.nasa.gov/mission/xmm-newton/, accessed: 15 June 2025.

79. Turner, M. J. L., A. Abbey, M. Arnaud, M. Balasini, M. Barbera, E. Belsole, P. J. Bennie, J. P. Bernard, G. F. Bignami, M. Boer, U. Briel, I. Butler, C. Cara, C. Chabaud, R. Cole, A. Collura, M. Conte, A. Cros, M. Denby, P. Dhez, G. Di Coco, J. Dowson, P. Ferrando, S. Ghizzardi, F. Gianotti, C. V. Goodall, L. Gretton, R. G. Griffiths, O. Hainaut, J. F. Hochedez, A. D. Holland, E. Jourdain, E. Kendziorra, A. Lagostina, R. Laine, N. La Palombara, M. Lortholary, D. Lumb, P. Marty, S. Molendi, C. Pigot, E. Poindron, K. A. Pounds, J. N. Reeves, C. Reppin, R. Rothenflug, P. Salvetat, J. L. Sauvageot, D. Schmitt, S. Sembay, A. D. T. Short, J. Spragg, J. Stephen, L. Strüder, A. Tiengo, M. Trifoglio, J. Trümper, S. Vercellone, L. Vigroux, G. Villa, M. J. Ward, S. Whitehead and E. Zonca, "The European Photon Imaging Camera on XMM-Newton: The MOS Cameras", *Astronomy & Astrophysics*, Vol. 365, pp. L27–L35, 2001.

80. XMM-Newton Science Operations Centre, European Space Agency (ESA), *XMM-Newton Users Handbook, Issue 2.23*, 2025.

81. Strüder, L., Briel, U., Dennerl, K., Hartmann, R., Kendziorra, E., Meidinger, N.,

Pfeffermann, E., Reppin, C., Aschenbach, B., Bornemann, W., Bräuninger, H., Burkert, W., Elender, M., Freyberg, M., Haberl, F., Hartner, G., Heuschmann, F., Hippmann, H., Kastelic, E., Kemmer, S., Kettenring, G., Kink, W., Krause, N., Müller, S., Oppitz, A., Pietsch, W., Popp, M., Predehl, P., Read, A., Stephan, K. H., Stötter, D., Trümper, J., Holl, P., Kemmer, J., Soltau, H., Stötter, R., Weber, U., Weichert, U., von Zanthier, C., Carathanassis, D., Lutz, G., Richter, R. H., Solc, P., Böttcher, H., Kuster, M., Staubert, R., Abbey, A., Holland, A., Turner, M., Balasini, M., Bignami, G. F., La Palombara, N., Villa, G., Buttler, W., Gianini, F., Lainé, R., Lumb, D. and Dhez, P., "The European Photon Imaging Camera on XMM-Newton: The pn-CCD camera", *Astronomy & Astrophysics*, Vol. 365, No. 1, pp. L18–L26, 2001.

82. XMM-Newton Science Operations Centre, European Space Agency (ESA), 2024, "Current Calibration Files (CCF) for XMM-Newton", `https://www.cosmos.esa.int/web/xmm-newton/current-calibration-files`, accessed: 15 June 2024.

83. Snowden, S. L. and Kuntz, K. D., 2023, "Cookbook for Analysis Procedures for XMM-Newton EPIC Observations of Extended Objects and the Diffuse Background", `https://heasarc.gsfc.nasa.gov/docs/xmm/esas/cookbook/xmm-esas.html`, accessed: 15 June 2023.

84. National Aeronautics and Space Administration (NASA)/CXC, 2019, "Chandra in Space (20 Years Illustration)", `https://www.nasa.gov/mission/chandra-x-ray-observatory/`, accessed: 15 May 2024.

85. Weisskopf, M. C., B. Brinkman, C. Canizares, G. Garmire, S. Murray and L. P. Van Speybroeck, "An Overview of the Performance and Scientific Results from the Chandra X-Ray Observatory", *Publications of the Astronomical Society of the Pacific*, Vol. 114, No. 791, p. 1, 2002.

86. Weisskopf, M. C., "The Chandra X-Ray Observatory: Progress Report and Highlights", *Proceedings of SPIE, the International Society for Optical Engineer-*

*ing/Proceedings of SPIE*, Vol. 8443, p. 84430Y, 2012.

87. Weisskopf, M., H. Tananbaum, L. Speybroeck and S. O'Dell, "Chandra X-ray Observatory (CXO): Overview", *Proc SPIE*, Vol. 4012, 2000.

88. National Aeronautics and Space Administration (NASA)/CXC, 2024, "Chandra X-ray Observatory Labeled Spacecraft Diagram", `https://www.nasa.gov/chandra-spacecraft-and-instruments/`, accessed: 20 May 2024.

89. Chandra X-ray Center, 2025, "CIAO Science Threads", `https://cxc.harvard.edu/ciao/threads/`, accessed: 6 April 2025.

90. Parekh, V., T. F. Laganá, K. Thorat, K. Van Der Heyden, A. Iqbal and F. Durret, "A Rrare Case of FR I Interaction with a Hot X-ray Bridge in the A2384 Galaxy Cluster", *Monthly Notices of the Royal Astronomical Society*, 2019.

91. European Space Agency (ESA), 2020, "Bridge Between Galaxy Clusters in Abell 2384", `https://www.esa.int/ESA_Multimedia/Images/2020/05/Bridge_between_galaxy_clusters_in_Abell_2384`, accessed: 15 May 2025.

92. Chandra X-ray Center, 2025, "Chandra Search and Retrieval (ChaSeR)", `https://cda.harvard.edu/chaser/`, accessed: 18 June 2025.

93. Freeman, P. E., V. Kashyap, R. Rosner and D. Q. Lamb, "A Wavelet-Based Algorithm for the Spatial Analysis of Poisson Data", *The Astrophysical Journal Supplement Series*, Vol. 138, No. 1, pp. 185–218, 2002.

94. Kaastra, J. S. and J. A. M. Bleeker, "Optimal Binning of X-ray Spectra and Response Matrix Design", *Astronomy & Astrophysics*, Vol. 587, p. A151, 2016.

95. Bekhti, N. B., L. Flöer, R. Keller, J. Kerp, D. Lenz, B. Winkel, J. Bailin, M. R. Calabretta, L. Dedes, H. A. Ford, B. K. Gibson, U. Haud, S. Janowiecki, P. M. W. Kalberla, F. J. Lockman, N. M. McClure-Griffiths, T. Murphy, H. Nakanishi, D. J.

Pisano and L. Staveley-Smith, “HI4PI: A Full-sky HI Survey Based on EBHIS and GASS”, *Astronomy & Astrophysics*, Vol. 594, p. A116, 2016.

96. Asplund, M., N. Grevesse, A. J. Sauval and P. Scott, “The Chemical Composition of the Sun”, *Annual Review of Astronomy and Astrophysics*, Vol. 47, No. 1, pp. 481–522, 2009.

97. NASA/IPAC Extragalactic Database (NED), 2024, “NED: NASA/IPAC Extragalactic Database”, `https://ned.ipac.caltech.edu`, accessed: 15 April 2025.

98. HEASARC, 2024, “nH Column Density Calculator”, `https://heasarc.gsfc.nasa.gov/cgi-bin/Tools/w3nh/w3nh.pl`, accessed: 15 April 2025.

99. Rasia, E., S. Borgani, G. Murante, S. Planelles, A. M. Beck, V. Biffi, C. Ragone-Figueroa, G. L. Granato, L. K. Steinborn and K. Dolag, “Cool Core Clusters From Cosmological Simulations”, *The Astrophysical Journal Letters*, Vol. 813, No. 1, p. L17, 2015.

100. Bulbul, G. E., R. K. Smith, A. Foster, J. Cottam, M. Loewenstein, R. Mushotzky and R. Shafer, “High Resolution XMM-Newton Spectroscopy of the Cooling Flow Cluster A3112”, *The Astrophysical Journal*, Vol. 747, No. 1, p. 32, 2012.

101. De Plaa, J., N. Werner, J. A. M. Bleeker, J. Vink, J. S. Kaastra and M. Méndez, “Constraining Supernova Models Using the Hot Gas in Clusters of Galaxies”, *Astronomy and Astrophysics*, Vol. 465, No. 2, pp. 345–355, 2007.

102. Roettiger, K., C. Loken and J. O. Burns, “Numerical Simulations of Merging Clusters of Galaxies”, *The Astrophysical Journal Supplement Series*, Vol. 109, No. 2, pp. 307–332, 1997.